

Univerzita Karlova v Praze
Přírodovědecká fakulta

Katedra fyzikální a makromolekulární chemie
Modelování chemických vlastností nano- a biostruktur



Mgr. et Ing. Eva Pluhařová

**Solvent effects on ion pairing and
photoionization in water**

**Vliv rozpouštědla na iontové párování a
fotoionizaci ve vodě**

Disertační práce

Ústav organické chemie a biochemie, AV ČR, v.v.i.
Centrum biomolekul a komplexních molekulových systémů

Školitel: Prof. Mgr. Pavel Jungwirth, DSc.

Praha 2014

First, I would like to thank my advisor, Pavel Jungwirth, for guiding me through the field of theoretical and computational chemistry, which was the best experience that could happen to me as a young scientist. I spent my graduate studies in a truly pleasant and lively environment created by my colleagues, especially Jana. I am also very grateful for having a chance to work with the research groups of Petr Slavíček, Burkhard Schmidt, Chris Mundy, Steve Bradforth, and Bernd Winter. Without them the completion of my thesis would not have been possible.

I would like to express many thanks to my parents for their support and love. Finally, thanks, Honza; I hope our long term experimental project never ends.

Prohlášení:

Prohlašuji, že jsem závěrečnou práci zpracovala samostatně a že jsem uvedla všechny použité informační zdroje a literaturu. Tato práce ani její podstatná část nebyla předložena k získání jiného nebo stejného akademického titulu.

V Praze, 26. června 2014

Eva Pluhařová

Title: Solvent effects on ion pairing and photoionization in water

Author: Mgr. et Ing. Eva Pluhařová

Department: Physical and Macromolecular Chemistry

Advisor: Prof. Pavel Jungwirth, DSc., IOCB AS CR, v.v.i.

Advisor's e-mail address: pavel.jungwirth@uochb.cas.cz

Abstract: Various methods of theoretical chemistry, namely classical molecular dynamics simulations with empirical force fields, *ab initio* molecular dynamics, enhanced sampling methods, and *ab initio* calculations were used to provide new insight into ion pairing and photoionization in aqueous solutions. Systems modeling aqueous solutions of decreasing size were investigated by computational methods of increasing level of sophistication.

In a classical molecular dynamics study of concentrated lithium salt solutions, the electronic continuum correction to account for polarization provided qualitative improvement over the conventional non-polarizable force fields and enabled molecular interpretation of neutron scattering measurements. The same modeling approach was also successful in predicting the affinity of halide ions to the solution/oil interface.

By combining *ab initio* molecular dynamics and potential of mean force calculations, we designed a reliable computational protocol for calculating the free energy profile for an ion pair dissociation. Further, we estimated the differences in the strength of Na⁺ and Ca²⁺ binding to the peptide bond employing umbrella sampling and found different geometries of the contact pairs for the two ions. Finally, we investigated the interplay between a neutral state and a strong salt bridge on one side and a strong and weak salt bridge on the other side for a model dipeptide.

Next, we studied photoionization of DNA in its native aqueous environment. First, we described the ultrafast formation and subsequent transformation of a cationic hole in water in the context of indirect radiation damage to DNA. Then, we predicted photoelectron spectra of nucleic acid components by *ab initio* calculations together with a nonequilibrium polarizable continuum solvent model, results of which were in a good agreement with experiment. Comparison with gas phase calculations showed a remarkable ability of the aqueous solvent to screen the electrostatic interactions. In addition, a very small change in the base ionization energy upon placing it into a piece of DNA again points to a major contribution of water to the overall environmental effect.

To summarize, presented results shed new light into molecular interpretation of ion pairing, ion specific Hofmeister effects, and radiation damage of DNA.

Keywords: ion pairing, DNA, photoionization, molecular dynamics, *ab initio* calculations, solvation.

Název práce: Vliv rozpouštědla na iontové párování a fotoionizaci ve vodě

Autor: Mgr. et Ing. Eva Pluhařová

Katedra: Fyzikální a makromolekulární chemie

Vedoucí doktorské práce: Prof. Mgr. Pavel Jungwirth, DSc., ÚOCHB AV ČR, v.v.i.

E-mail vedoucího: pavel.jungwirth@uochb.cas.cz

Abstrakt: Různé metody teoretické chemie, konkrétně klasická molekulová dynamika s empirickými silovými poli, *ab initio* molekulová dynamika, metody rozšířeného vzorkování a *ab initio* výpočty, byly použity k hlubšímu pochopení iontového párování a fotoionizace ve vodných roztocích. Zmenšující se modelové systémy byly zkoumány výpočetními metodami rostoucí přesnosti a náročnosti.

Při studiu koncentrovaných roztoků lithných solí klasickou molekulovou dynamikou vedla oprava zahrnující elektronické kontinuum ke kvalitativnímu zlepšení oproti konvenčním nepolarizovatelným silovým polím, a tak umožnila interpretaci měření pomocí rozptylu neutronů. Stejný přístup byl také úspěšný pro předpověď afinity halidů k rozhraní voda/olej.

Kombinací *ab initio* molekulové dynamiky a výpočtů potenciálu střední síly byl navržen spolehlivý postup pro výpočet profilu volné energie pro disociaci iontového páru. Poté byly odhadnuty rozdíly v síle interakce Na^+ a Ca^{2+} s peptidovou vazbou pomocí “deštníkového vzorkování” a byly popsány různé geometrie kontaktních párů pro oba ionty. Nakonec byla v modelovém dipeptidu zkoumána rovnováha mezi neutrální formou a silným solným můstkem na jedné straně a silným a slabým solným můstkem na druhé straně.

Dále byla studována fotoionizace DNA v přirozeném vodném prostředí. Nejprve byla popsána ultrarychlá tvorba a následná přeměna kationtové díry ve vodě v kontextu nepřímého radiačního poškození DNA. Pak byla předpovězena fotoelektronová spektra složek nukleových kyselin pomocí *ab initio* výpočtů a nerovnovážného polarizovatelného dielektrického modelu roztoku. Získané výsledky byly v souladu s experimentem. Srovnání s výpočty v plynné fázi ukázalo značnou schopnost rozpouštědla odstínit elektrostatické interakce. Hlavní podíl vody v celkovém vlivu prostředí se navíc projevil jako velmi malá změna ionizační energie báze při jejím umístění do kusu DNA.

Všechny zmíněné studie přispěly k osvětlení molekulové interpretace iontového párování, iontově specifických Hofmeisterových efektů a radiačního poškození DNA.

Klíčová slova: iontové párování, DNA, fotoionizace, molekulová dynamika, *ab initio* výpočty, solvatace.

Contents

1	Introduction	1
2	Methods	4
2.1	Sampling	5
2.2	Selected topics in neutron scattering	7
2.3	Empirical force fields	9
2.4	<i>Ab initio</i> molecular dynamics	10
2.5	Changing number of electrons in solution	12
2.5.1	Modeling photoionization spectrum	12
2.5.2	Modeling solvation	14
2.6	Photoelectron spectroscopy	17
3	Improving force fields for concentrated salt solutions	19
3.1	Ion pairing in lithium salt solutions	19
3.2	Aqueous interfaces	26
4	Ion pairing by <i>ab initio</i> molecular dynamics	29
4.1	LiF ion pair	30
4.2	N-methylacetamide with cations	33
4.3	Dipeptide salt bridge	36
5	DNA damage by ionizing radiation	41
5.1	Cationic hole in water	43
5.2	Direct ionization of DNA components	45
5.3	Ionization of a piece of DNA	51
6	Conclusions	55
	List of Abbreviations	58

Bibliography	60
List of Attached Publications	69
Attached Publications	70

Chapter 1

Introduction

Biologically relevant chemical processes take place, as a rule, in aqueous solutions and water plays an important role in many of them. More specifically, water is needed by all known forms of life, therefore, it is called the universal solvent in biology. A solution consists of a solvent which is the major component and can be said to create the environment for a solute that is minor in composition, but receives more attention. The influence of the solvent varies from providing just a “cage”, where the solute is held, over creating a polarizable medium which affects the electronic structure properties of the solute, to an important part of the reaction coordinate in addition to the intuitively chosen solute coordinates, which can take place either without or with breaking of the bonds of solvent molecules.

Although my work is theoretical and computational, a large part of it was motivated by collaboration with experimentalists or by unexplained differences between theoretical and experimental studies done so far. This thesis focuses on two phenomena - ion pairing and photoionization which will be shortly introduced in the following paragraphs. Ion pairing in electrolyte solutions means association of oppositely charged ions without formation of a covalent bond [1]. Coulomb attraction competes with tendency for water to solvate charges separately, thereby shielding them to a certain extent. In order to rationalize thermodynamic properties of salt solutions, such as density, osmotic pressure, activity coefficients, or kinetic behavior, several models have been developed during the past century [1–4]. Bjerrum originally suggested that all oppositely charged pairs of ions closer than a certain distance should be treated as associated ion pairs, whereas those at larger distances should be considered as free [1, 2]. On the other hand, the widely used Pitzer’s model of interacting ions was able to provide thermodynamic properties such as activity coefficients without considering ion pairing explicitly [4, 5]. Nowadays, arrangement of

ions in solution can often be deduced from modern spectroscopic techniques [6–12]. One of them, neutron scattering with isotopic substitution, has been performed by our colleagues in Grenoble.

The most prominent ion pairs in biochemistry, salt bridges, occur between titratable amino acid side chains in proteins and their role in stabilizing the protein structure is still subject of scientific discussion [13–17]. Furthermore, the solubility of peptides and proteins in aqueous environments is influenced by ions. The effect of different salts was first classified by Franz Hofmeister [18]. The explanation of the molecular mechanism is still an active area of research, being based on quantifying the different strengths of ion-water, ion-protein, and protein-water interaction. Classical molecular dynamics (MD) with empirical force fields (FF) is a powerful tool for rationalization of problems mentioned above, but the predictions are sometimes too sensitive to the details of the empirical FF. Then, *ab initio* MD is the method of choice.

The other phenomenon under study is photoionization, which means ejecting an electron, characterized by its ionization energy (IE), from a molecule by a photon that has an equal or higher energy $h\nu$. Ionization characteristics of nucleic acid components help us in understanding the radiation damage of DNA, which can be ionized directly by incoming photon or damaged indirectly by products resulting from ionization of the molecules in the surrounding. Many studies have investigated molecules in the gas phase employing both photoelectron spectroscopy and *ab initio* calculations, but the influence of aqueous medium including ions should be also taken into account. Photoelectron spectroscopy experiments on aqueous species became possible about ten years ago [19] thanks to the microjet technique and they are performed extensively by our collaborators in Berlin. Theoretical modeling of solvent effects on photoionization is non-trivial due to the need of combining reasonable level of theory and appropriate model of solvation.

This thesis is organized as follows. Chapter 2 outlines theoretical methods employed in this study and also contains two experimental sections: the first one about neutron scattering with isotopic substitution which is closely connected to the structure of solution characterized by radial distribution functions, and the second one about photoelectron spectroscopy. Results sections start in Chapter 3 with chemically relatively simple concentrated salt solutions studied by neutron scattering and classical MD with empirical force fields, that needed to be refined. Although such simulations provide useful molecular picture for the measurements, sometimes a more accurate and less parameter-dependent description is needed. Therefore, in Chapter 4, we use computationally more demanding *ab initio* MD on smaller systems. The

aims are to study exact energetics of an ion pair dissociation in bulk water, a peptide-bond – cation interaction, and structure and dynamics of a peptide salt bridge in differently hydrated environment. Chapter 5 is dedicated to the radiation damage of DNA. It starts with a short section about the first step of indirect damage of DNA, i.e., creation of a “cationic hole” in water after photoionization. This part is followed by description of ionization characteristics of individual building blocks: bases, nucleosides, differently protonated phosphate ions, differently protonated nucleotides, and also one product of the radiation damage. I investigated some of the species already in my diploma thesis, but the calculations were extended here and summary of these results will help to provide a complete picture of direct DNA damage. Next, we discuss which other properties (such as redox potentials) can be derived from ionization energies. Finally, we try to answer the question about how relevant are the ionization energies of individual components for a piece of DNA. All calculations are closely related to experimental results from photoelectron spectroscopy. The chapters are organized according to the increasing level of accuracy and sophistication of theory employed for the description of the systems. They always contain discussion about sampling of the representative structures and how can the effect of the solvent be viewed in each case. Finally, Chapter 6 summarizes the main findings.

Chapter 2

Methods

This chapter provides a brief overview of methods, mainly theoretical, but also experimental, used in this thesis. All calculations rely on the Born-Oppenheimer approximation, which is based on the fact that atomic nuclei are much heavier than electrons and it is, therefore, possible to assume that electrons are moving infinitely fast in the field of fixed nuclei. In MD simulations that we have performed, equations of motions for atoms are always classical, i.e., Newton ones. Forces acting on atoms are derived from empirical force fields or from solving approximate electronic Schrödinger equation for given positions of nuclei, depending on the character of the problem.

One of the main goals of theoretical chemistry is to make a connection between simulated quantities and macroscopic observables of systems studied, but is not necessary and even not possible to apply microscopic laws of motion to a system containing about $6 \cdot 10^{23}$ particles [20]. Therefore, the first step is the choice of an appropriate model system, phase space of which could be sampled sufficiently. The reliability of sampling is related to the statistical error of the calculation. The other source of uncertainties, i.e., systematic ones, comes from the level of approximate theory at which energy of the system is evaluated; this can be benchmarked against higher level methods or experiment. In order to obtain meaningful results, both types of uncertainties, as well as the model system size have to be under control in a balanced way, which may of course lead to serious compromises.

The ordering of the topics presented here differs from what the reader may be used to because of large variety of system sizes and theoretical methods employed. We start with discussing sampling of the phase space and analysis of the simulated data, which are then related to the experimental determination of structure of aqueous solutions by neutron scattering. Sections 2.3 and 2.4 provide details about evaluation

of forces between molecules in classical and *ab initio* MD. Next, we have to improve the level of theory up to the point where it is able to capture changes in the number of electrons in the system, and, at the same time significantly simplify description of the solvent. The last section thus deals with photoelectron spectroscopy in aqueous solutions.

2.1 Sampling

Statistical thermodynamics allows us in principle to determine macroscopic properties from knowledge of microscopic interactions through partition function Q of a particular ensemble. Such calculations are, however, computationally intractable, therefore, we calculate thermodynamic quantities in a different way.

How to choose the size of the model system and find representative structures? Sometimes, a system consisting of a single molecule is satisfactory and, moreover, it is sufficient to take into account only the global or several local minima when exploring the configuration space. This approach is used when modeling photoelectron spectra of isolated gaseous molecules and even species in aqueous solution, when it is possible to approximate the solvent as a polarizable dielectric continuum. For larger systems, molecular dynamics is a more appropriate sampling technique.

MD stands for numerically solving equations of motion for microscopic representative systems [20]. Assuming we know the interaction potential, we can calculate the potential energy U of a system containing N atoms and evaluate the force by taking the negative derivative of it with respect the atomic coordinate r_I . The system evolves in time according to the Newton equation of motion:

$$\ddot{\mathbf{r}}_I = \frac{\mathbf{f}_I}{M_I} = -\frac{1}{M_I} \frac{\partial U(\mathbf{r}^N)}{\partial \mathbf{r}_I}, \quad (2.1)$$

Classical MD may be employed to study systems containing thousands of atoms for hundreds of nanoseconds. These are not really macroscopic dimensions, but they are able to capture many properties. This number of particles would not be, however, sufficient for description of a condensed phase, therefore, in order to remove surface effects the periodic boundary conditions (PBC) are applied. Summation of contributions to potential energy over infinite number of periodic images is not performed in a naive way. Instead, for potentials decaying faster than r^{-3} cut off is used, while for long-range potentials, where the summation has to be performed, special methods, such as the Ewald summation, are employed [21, 22]. We usually intend

to study systems at constant temperature and volume or pressure, i.e., the NVT or NpT ensembles. In order to generate them instead of the microcanonical ensemble, the temperature and pressure in the latter case have to be constrained by additional algorithms.

How to analyze the collected trajectory in a way that is easy to understand and visualize? The basic structural quantity is the pair correlation function $g(\mathbf{r}_1, \mathbf{r}_2)$ which is the normalized probability density of finding a pair of particles in the configuration $\mathbf{r}_1, \mathbf{r}_2$ independently of the other particles. For a single component system in the NVT ensemble it reads:

$$g(\mathbf{r}_1, \mathbf{r}_2) = \frac{N \cdot (N - 1)}{\rho^2 Z_{NVT}} \int \dots \int e^{\frac{-U(\mathbf{r}_1, \mathbf{r}_2, \dots, \mathbf{r}_N)}{k_B T}} d\mathbf{r}_3 \dots d\mathbf{r}_N \quad (2.2)$$

where \mathbf{r}_i are the position vectors, k_B is the Boltzmann constant, T is the absolute temperature, ρ the average particle density and Z_{NVT} is the configuration integral, which is obtained from partition function Q_{NVT} after integration over momenta and serves here as a normalization constant. In homogeneous systems, only the relative position $\mathbf{r}_1 - \mathbf{r}_2$ is relevant, so the \mathbf{r}_2 is integrated out. In Chapter 4, the resulting $g(\mathbf{r}_1, \mathbf{r}_2) \equiv g(\mathbf{r})$ is called the spatially resolved distribution function or density map. The widely used radial distribution function $g(r)$ is obtained from $g(\mathbf{r})$ by integrating over angular coordinates. It is related to molecular interactions via Eq. 2.2 and from the collected trajectory it can be evaluated as:

$$g(r) = \frac{V}{N(N-1)} \left\langle \sum_i \sum_{j \neq i} \frac{\delta(r - r_{ij})}{4\pi r^2} \right\rangle, \quad (2.3)$$

where brackets denote the time average.

If thermodynamically converged results cannot be obtained by direct sampling in the limited simulation time, we opt for so called free energy methods, which no more provide dynamical information, but visit adequately regions (almost) inaccessible by the direct method. The Helmholtz free energy A is related to the canonical partition function by $A = -k_B T \ln(Q_{NVT})$. The free energy profile along a coordinate r analogously reads:

$$W(r) = -k_B T \ln g(r), \quad (2.4)$$

where $W(r)$ is the potential of mean force (PMF), because it can be shown that it is an integral of a mean force acting between selected particles averaged over the

others. The following paragraph describes how to get the free energy profile as an integral of mean force, while the last paragraph shows an alternative approach.

Calculating the free energy profile along a selected reaction coordinate r , eg. ion-ion distance, as an integral of mean force consists of series of independent simulations, in which the distance is fixed (constrained) at different values of r in each case. The time average of the force acting between particles at a constrained distance is evaluated and then integrated:

$$W(r) = - \int_{r_0}^r \bar{F}(r') dr' + 2 \cdot k_B T \ln(r/r_0) + C, \quad (2.5)$$

where r_0 is a reference point, the second term is the entropic correction due to the different volumes of the phase space sampled in individual sampling windows and C is an integration constant.

An alternative approach for getting the free energy profile is the so called umbrella sampling method, where instead of constraining the reaction coordinate, it is restrained with a biasing potential usually having a harmonic form. The protocol also consists of a series of simulations sampling different areas of reaction coordinate. From each simulation window, biased probability distributions are obtained, which have to be unbiased and glued together to get a full probability distribution. To this end, we employ the weighted histogram analysis method (WHAM) [23].

2.2 Selected topics in neutron scattering

In the previous section, we introduced the concept of the radial distribution function which can be easily calculated from the MD trajectories, provides insight into the structure of the investigated system, and on top that, all non-entropic thermodynamic functions can be evaluated employing it assuming pair additivity of the interactions [24]. It is not possible to get it directly from experiments, but it is closely related to a measurable quantity, the structure factor. Structural data of aqueous solutions can be obtained by either neutron scattering or X-ray diffraction. Neutron scattering has a good ability to resolve hydrogens, which tend to be almost invisible in x-ray scattering due to the low number of electrons. Since Chapter 3 provides combined theoretical and experimental study of concentrated salt solutions, basic principles of the neutron scattering technique are mentioned in the following paragraphs, although the author never performed any neutron scattering experiment herself.

The total static structure factor $S(Q)$ is related to the angular dependence of the intensity of the radiation scattered by the sample:

$$S(Q) = \frac{1}{N} \sum_{j,k} b_j b_k \langle e^{iQ|\mathbf{r}_j - \mathbf{r}_k|} \rangle, \quad (2.6)$$

where b_j is the scattering length, \mathbf{r}_j the position of the atom j , and N is the total number of atoms in the system studied. The averaging is performed over all possible orientations of the wave vector Q compared to the vector $\mathbf{r}_j - \mathbf{r}_k$. $S(Q)$ can be written as:

$$S(Q) = \sum_{\alpha,\beta} c_\alpha c_\beta b_\alpha b_\beta (S_{\alpha\beta}(Q) - 1), \quad (2.7)$$

where $c_\alpha = N_\alpha/N$ is the atomic concentration of the species α , $S_{\alpha\beta}(Q)$ is the partial structure factor, and the summations run over all atomic species in the solution. The partial structure factor is related to the radial distribution function via Fourier transform:

$$g_{\alpha\beta}(r) - 1 = \frac{V}{2\pi^2 N r} \int_0^\infty (S_{\alpha\beta}(Q) - 1) Q \sin(Qr) dQ. \quad (2.8)$$

Other structural functions that are useful for comparison of simulated and experimental results can be introduced, e.g., $G(r)$ which reads:

$$G(r) = \sum_{\alpha,\beta} c_\alpha c_\beta b_\alpha b_\beta (g_{\alpha\beta}(r) - 1). \quad (2.9)$$

The total scattering pattern starts to be complicated already for a simple electrolyte containing atomic cations M^+ and atomic anions X^- , because it has 10 contributions (HH, HO, HM, HX, OO, OM, OX, MM, MX, and XX) out of which those containing hydrogen (followed by oxygen) dominate due to the scattering length and concentration reasons. In order to reduce the number of partial structure factors and also make the ones containing electrolyte atoms detectable, the technique of Neutron Diffraction with Isotopic Substitution (NDIS) has been developed [25]. This technique consists of measurement of total neutron scattering patterns from two chemically identical solutions which vary only in the isotopic concentration of the substituted nucleus, for example X. By subtracting these two scattering patterns,

contributions like HH, HO, etc. are canceled and it is possible to obtain the structure of solution around the substituted X nuclei which in our example contains only 4 partial structure factors.

2.3 Empirical force fields

So far we have not mentioned how to evaluate the potential energy of the system, which is needed when applying the methodology of statistical thermodynamics, e.g., equation 2.2 or when propagating the Newton equation of motion (Eq. 2.1). Nowadays, the majority of MD simulations is performed using non-polarizable empirical force fields (FF), which despite simplifications have been quite successful for description of complex molecular systems [26], if bond breaking or making does not occur. Atoms are treated as “elementary particles” and the interactions among them are described by empirical formulas. The total energy is divided into bonded (intramolecular) and non-bonded (intermolecular) contributions. The former part is usually decomposed into the bond, angle, and dihedral contributions, the first two being frequently modeled within harmonic approximation, the last one is expanded in a Fourier series. The intermolecular interactions are described via electrostatic (fixed partial charges on atoms), dispersion, and repulsion terms (e.g., Lennard-Jones or Buckingham potentials). The parameters of the formulas are optimized to reproduce target properties such as the enthalpy of solvation, the enthalpy of vaporization, dipole moment, spectroscopic data, or results of independent electronic structure calculations.

There are still problems even with non-reactive systems, e.g., in the simulation of polarization effects. The non-polarizable models can significantly underestimate the magnitude of the dielectric response in low-dielectric protein environment [27,28] and lipid membranes [29]. This can be partially solved by polarizable FFs, that involve coupled polarizable sites which, however, makes them computationally more demanding and thus still not applicable to many biological systems. Therefore, the approximations behind the current non-polarizable models still need to be better understood which can then also allow for including polarizability under certain conditions in an approximate way (see below).

An important issue related to non-polarizable models is parametrization of water. It has been suggested that partial charges of empirical water models are effective charges which reflect the omission of explicit polarizability, namely showing that the effective water dipole μ^{eff} can be understood as a scaled value $\mu^{eff} = \mu / \sqrt{\epsilon_{el}}$, where

$\epsilon_{el} = 1.78$ is the electronic (high-frequency) part of the dielectric constant of water [30, 31]. This leads to an idea of a uniform electronic continuum, with an effective dielectric constant and point charges moving in it. The electronic polarizability of ions responds instantaneously to the external field, which is represented here by the field of point atomic charges. Since water partial charges have already been effectively scaled, all that remains is to scale the ionic charges $q_i^{eff} = q_i/\sqrt{\epsilon_{el}}$ [32]. This ‘‘Electronic Continuum Correction’’ (ECC) makes the treatment of electrostatic interactions between the solute and the solvent more balanced.

However, the employed methodology is only approximate and our results cannot be better than the force field. If large discrepancies between the predictions of simulations and experiment (e.g., section 3.1) remain, even if the sampling is converged (section 2.1), this implies that the force field employed is not able to capture all the complexities of the system. In these cases we have to opt for electronic structure methods for evaluating interactions, which is the subject of the next section.

2.4 *Ab initio* molecular dynamics

In *ab initio* molecular dynamics (AIMD), atomic nuclei are treated classically, meaning that they move according to Newton’s equations of motion. However, forces acting on nuclei are obtained as derivatives of energy (Eq. 2.10) which is the solution of an appropriate approximation of the time-independent electronic Schrödinger equation (Eq. 2.11).

$$M_I \ddot{\mathbf{R}}_I(t) = -\nabla_I E_0(\mathbf{R}) \quad (2.10)$$

$$\hat{H}_{el}\psi_0 = E_0\psi_0 \quad (2.11)$$

In this thesis we used the Born-Oppenheimer (BO) scheme, where the ground state electronic structure problem is solved iteratively in each MD step for given nuclear coordinates. Such calculations are computationally demanding, therefore, efficient density functional theory (DFT) methods are employed in most of the BOMD studies nowadays.

A stationary electronic state is characterized by a wave function ψ which depends on coordinates of all electrons and parametrically on nuclear coordinates. DFT allows for a description based on a simpler object - electron density $n(\mathbf{r})$ depending only on three spatial coordinates. DFT is a formally exact ground state theory, but the exact

energy functional $E[n]$ is not known. The total electron energy consists of electron kinetic energy $E^T[n(\mathbf{r})]$, electron-electron interaction energy $E^{V_{ee}}[n(\mathbf{r})]$ and electron interaction with a potential v generated by the nuclei $E^{V_{ne}}[n(\mathbf{r})] = \int n(\mathbf{r})v(\mathbf{r})d\mathbf{r}$:

$$E[n(\mathbf{r})] = E^T[n(\mathbf{r})] + E^{V_{ee}}[n(\mathbf{r})] + E^{V_{ne}}[n(\mathbf{r})]. \quad (2.12)$$

Kohn and Sham proposed a reference system of non-interacting electrons, that generates the same density as the system of interacting particles. Using Kohn-Sham orbitals ϕ_i it is possible to evaluate the kinetic energy of the reference system efficiently. The energy expression is then rewritten in the following way (in atomic units):

$$E[n(\mathbf{r})] = \sum_i \langle \phi_i | -\frac{1}{2}\nabla^2 | \phi_i \rangle + \frac{1}{2} \int \frac{n(\mathbf{r})n(\mathbf{r}')}{|\mathbf{r} - \mathbf{r}'|} d\mathbf{r}d\mathbf{r}' + \int n(\mathbf{r})v(\mathbf{r})d\mathbf{r} \\ + E^{xc}[n(\mathbf{r})], \quad (2.13)$$

where $E^{xc}[n(\mathbf{r})]$ is the unknown exchange-correlation energy, which consists of non-classical part of the electron-electron interaction and the difference between the kinetic energy of the system of interacting particles and the reference system.

The DFT based BOMD studies have been made possible thanks to the algorithms implemented in the CP2K-QuickStep [33] program package. The key ingredient is the hybrid Gaussian (Eq. 2.14) and plane waves (Eq. 2.15) (GPW) representation of electron density.

$$n(\mathbf{r}) = \sum_{\mu\nu} P^{\mu\nu} \varphi_\mu(\mathbf{r})\varphi_\nu(\mathbf{r}), \quad (2.14)$$

where $P^{\mu\nu}$ is a density matrix element and φ_μ is an atom centered contracted Gaussian basis function. This representation is efficient for disordered molecular systems with high electron density in the vicinity of atomic nuclei and low density between molecules. But it is position dependent, nonorthogonal, and the evaluation of the Coulombic part of the electron-electron interaction requires evaluation of a large number of multi-center integrals. This energy term can be efficiently calculated using fast Fourier transform upon employing the plane wave basis set:

$$n'(\mathbf{r}) = \frac{1}{\Omega} \sum_{\mathbf{G}} n'(\mathbf{G})\exp(i\mathbf{G} \cdot \mathbf{r}). \quad (2.15)$$

Here \mathbf{G} are the reciprocal lattice vectors and Ω is the volume of the unit cell. The plane wave basis set is orthogonal, but inefficient in representation of atom-filled and empty regions. GPW approach combines advantages of both basis sets. The expansion coefficients $n'(\mathbf{G})$ are such that $n(\mathbf{r})$ and $n'(\mathbf{r})$ are equal on a regular grid in the unit cell.

Expansion of the all-electron density in plane waves is computationally demanding and sometimes even not feasible. In order to decrease computational cost and at the same time preserve the ability to describe chemically interesting processes, only valence electrons are described accurately. Nuclei and non-valence (core) electrons are encapsulated in a pseudopotential. In this work we used norm-conserving, separable dual-space Goedecker, Teter, Hutter (GTH) pseudopotentials [34], which consist of a local part, including a short-ranged and a long-ranged term, and a non-local part.

Energy contributions are computed in the following way. Analytic expression for kinetic energy is evaluated in a real space in the Gaussian basis set. Electrostatic energy terms in the periodic systems, which we are almost always studying, has to be treated simultaneously using Ewald sum method, i.e., the long range part in the Fourier space and the short range part in the real space. The exchange correlation functional is usually a function of the density and its gradient, so similar techniques for its evaluation as for Coulombic part of the electron-electron interaction are used.

2.5 Changing number of electrons in solution

In the previous methodological sections it was assumed that the studied system remains in its closed shell electronic ground state. This section describes how we face the challenging task of photoionization in aqueous solution. It requires treatment of the part of the system being ionized at an *ab initio* level, because number of electrons is changing, and at the same time account for solvation. It is impossible to treat the whole solution at an *ab initio* level, therefore, it is necessary to adopt serious compromises and understand the range of their validity.

2.5.1 Modeling photoionization spectrum

The object of this subsection is to briefly describe terms and computational methods that are needed for theoretical prediction of photoelectron spectra. We would like to know the energy difference between electronic states before and after ionization, i.e., ejecting an electron, as well as probabilities associated with such transitions.

Let us be guided by the Fermi golden rule Eq. 2.16 which was derived employing time dependent perturbation theory and gives photoionization cross-section σ as a function of the photon angular velocity ω [35]:

$$\sigma(\omega) = \left(\frac{\pi e^2 \omega}{3 \hbar \epsilon_0 c} \right) \sum_{f,i} \rho_i |\langle \psi_f | \hat{r} | \psi_i \rangle|^2 \delta \left(\omega - \frac{E_f - E_i}{\hbar} \right), \quad (2.16)$$

where ψ_i and ψ_f are the wave functions of the initial state and the final state, and E_i and E_f are their energies. Note that in case of ionization, final states are continuum states. ρ_i is the density of the initial state, \hat{r} is the operator of the direction of electric field, and e is the elementary charge. To model the photoelectron spectrum rigorously, we would have to calculate wave functions and corresponding energies by solving the time-independent Schrödinger equation and sample the initial state density employing molecular dynamics methods. In order to be able to describe ionization of medium size systems, e.g. nucleic acid (NA) bases, nucleosides, and nucleotides, a more approximate approach is adopted. The ground state energy of a closed-shell species before ionization was evaluated at the MP2/aug-cc-pVDZ level of theory, while the ground state energy of the species having one electron less was calculated employing the unrestricted version of the MP2 method with higher spin components annihilated via Schlegel’s projection method (PMP2) [36]. The difference of these two energies is the lowest ionization energy, IE_0 . Higher ionization energies, i.e., corresponding to ejection of more tightly bound electrons, can be in principle calculated by elaborate methods like ionization-potential equation-of-motion coupled cluster theory (IP-EOM-CC) [37,38] or by various electron propagator methods like outer valence Green’s function [39,40], partial third-order theory (P3) [40,41], and the algebraic diagrammatic construction (ADC) [40,42]. Here, we proceed in a simpler two step way as is illustrated in Fig. 2.1: We first calculate IE_0 and then excitation energies to singly occupied molecular orbital (SOMO) of ionized species employing TDDFT at the BMK/6-31+g* level. Adding excitation energy to the lowest ionization energy results in the corresponding IE . The PMP2/TDDFT concept gives a good estimate of ionization energies in comparison with the multireference CASPT2 method [43,44]

The photoionization cross section is not evaluated explicitly, but we take advantage of knowing the experimental setup which allows us to simplify the calculation. Namely, the energy of incoming photons is well above the ionization threshold, therefore, the same photoionization cross sections can be assigned to all transitions [43,45].

Photoelectron emission is broadened due to the uncertainty of the energy difference $E_f - E_i$. Depending on the nature of the uncertainty, i.e., whether each quantum

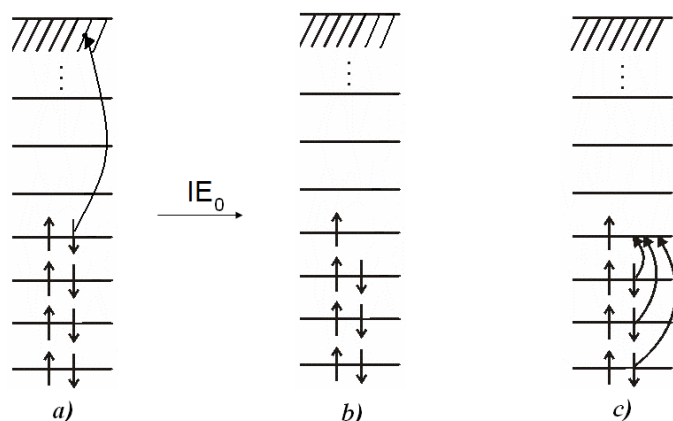


Figure 2.1. Calculation of ionization energies of lower lying electron via “indirect approach”. a) The ground state of a non-ionized closed shell particle, b) the ground state of an ionized open-shell particle, and c) excitations to SOMO within the ionized particle.

emitter has the same type of fluctuation or not, we distinguish homogeneous or inhomogeneous broadening. Homogeneous broadening does not contribute significantly to the band width in liquid water, while two types of inhomogeneous broadening, thermal and electronic, have more important roles [46]. The former one is related to the spread of the effective MO energies, because each molecule has different environment due to the thermal disorder, the latter one is related to the electronic interaction of a particular molecule with the surrounding solvent. The thermal and electronic broadening are comparable in magnitude, with the electronic being usually dominant in water. In addition to that, the influence of nuclear quantum delocalization on the shape of the PE spectra of water clusters was found to be more important than the thermal broadening [47].

For nucleic acid bases and their derivatives, all these contributions to the peak width are incorporated into a Gaussian with full width at half maximum of 1 eV which is appropriate for aqueous solution [19,43]. To get the theoretical photoelectron spectrum, each IE is thus convoluted with such a Gaussian and these Gaussians are summed up.

2.5.2 Modeling solvation

Solvation can be modeled via several alternative approaches illustrated in Fig. 2.2: a) microsolvation, b) combined quantum chemical/molecular mechanics method, c) continuum solvation, and d) hybrid model (explicit solvent plus continuum). In the first case, a cluster composed of the solute and a small number of water molecules

is described at an *ab initio* level. This approach captures specific effects within the first solvation shell, but it cannot account for long-range polarization of the solvent molecules by the solute. Convergence of properties of such clusters toward bulk is typically slow. In the second approach, more, sometimes hundreds, of solvent molecules are included, which are modeled using point charges. The solute and sometimes the closest solvent molecules are treated using *ab initio* methods.

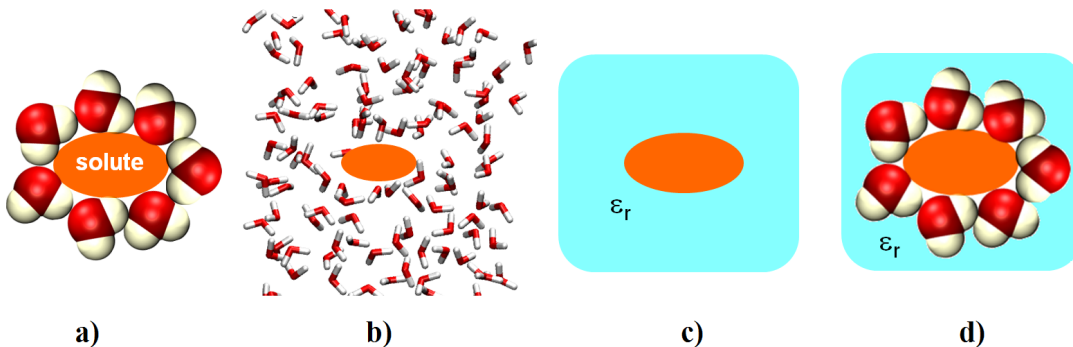


Figure 2.2. Models of solvation: a) microsolvation; b) mixed quantum chemical/molecular mechanics approach; c) continuum solvent model; d) hybrid model.

In continuum solvent models (Fig. 2.2 c), the solvent is simplified to a structureless polarizable infinite medium characterized by a dielectric constant giving a reasonable description of the solute-solvent interaction. The solute free energy is expressed as the following sum [48, 49]:

$$G = G_{el} + G_{cav} + G_{dis} + G_{rep}, \quad (2.17)$$

where cavitation free energy G_{cav} is the work required to create a cavity, G_{dis} and G_{rep} are the solute-solvent dispersion and repulsion interactions, and G_{el} is the electrostatic interaction which needs to be discussed in more details. All terms are calculated using a cavity formed by interlocking spheres centered on atoms or atomic groups, which is a generally adopted compromise between cavities that are too simple, e.g. spherical or ellipsoidal for the whole molecule, but analytically solvable, and realistic, but computationally expensive cavity shapes [50].

Upon solvation, the solute Hamiltonian (\hat{H}_{vacuum} in vacuo) becomes an “effective Hamiltonian” for the solute in the presence of a polarized dielectric:

$$\hat{H} = \hat{H}_{\text{vacuum}} + \hat{V}_{el}. \quad (2.18)$$

The electrostatic interaction operator \hat{V}_{el} depends on “solvation charges” q_i located at the surface of the cavity. Their determination starts from Poisson’s equation which is appropriate if the dielectric medium responds in a linear fashion to the embedding of charge. Having the solution of the Poisson’s equation under cavity boundary conditions and the solute charge density, an integral equation to determine the surface charge density can be written [50]. The cavity surface is discretized into small domains called “tesserae” which changes the integral equation for surface charge density to a set of coupled linear equations for q_i :

$$\mathbf{D}\mathbf{q} = -\mathbf{b}, \quad (2.19)$$

where \mathbf{b} contains the solute electrostatic potential or the solute normal electric field on the cavity surface, while \mathbf{D} depends on the solute dielectric constant ϵ and the cavity shape. Since the solute is polarized by the solvent and vice versa, the problem has to be solved iteratively.

In many applications, for example, in fast processes such as vertical excitations or ionization, we have to distinguish between two sources of the solvent polarization with very different relaxation times. The faster component (sometimes called optical or electronic) of the solvent polarization is expected to relax at the same speed as electronic motions, i.e., almost instantaneously, and it is considered always equilibrated to the solute, while the slower one (orientational, nuclear, or inertial) remains frozen during electronic transitions and responds with a time scale typical for nuclear motions [48, 49].

To model solvent effects during the fast electronic processes correctly, a so-called non-equilibrium PCM (NEPCM) calculation [48, 49] needs to be performed. Each solvation charge is split into two contributions, fast and slow:

$$q_i = q_{i,f} + q_{i,s}. \quad (2.20)$$

To determine the “slow” charges, which do not change during the fast process, the difference between total and the “fast” charges of the original state is evaluated. First both the “slow” and the “fast” polarization charges are determined for the ground state by solving two following equations:

$$\mathbf{D}(\epsilon)\mathbf{q} = -\mathbf{b}, \quad (2.21)$$

which is just Eq. 2.19 with explicitly written dependence on ϵ , and

$$\mathbf{D}(\epsilon_f)\mathbf{q}_f = -(\mathbf{b} + \mathbf{b}_s), \quad (2.22)$$

where \mathbf{b}_s represents the contribution generated by the “slow” charges. For the resulting state of the molecules, slow charges evaluated for the ground state are used and only “fast” polarization charges are recalculated. This method captures the long-range electronic polarization and performs well within the linear regime of the solvent response, because it was derived under this assumption.

For solutes with high charge density (e.g., multiply charged ions) or with strong specific interaction, the PCM model is not valid anymore. A possible extension is to solvate the solute with explicit solvent molecules and insert the whole complex into the polarizable continuum as is depicted in Fig. 2.2 d) hybrid model. Explicit solvent molecules create a “buffer” zone, so that treatment of the rest of the solvent as a linearly responding continuum becomes applicable.

2.6 Photoelectron spectroscopy

Since Chapter 5 provides results from a combined theoretical and experimental study of photoionization of aqueous species, basic principles of the experimental setup are mentioned in the following paragraphs, although the author never performed such experiments herself.

Photoelectron (PE) spectroscopy is an experimental technique which provides the detailed knowledge of the electronic structure of matter. It is based on the photoelectric effect, i.e., if photons of energy $h\nu$ interact with a particle having electrons of ionization energy $IE \leq h\nu$, ionization can occur. Kinetic energy of the ejected electrons E_K is given by

$$E_K = h\nu - IE = h\nu - (E_f - E_i), \quad (2.23)$$

where E_i is the energy of the non-ionized particle and E_f is the energy of the final state of the ionized particle. PE spectrum is the dependence of the photoelectron counts on the kinetic energy, optionally also on the angle between the incoming radiation and the outgoing photoelectron. In order to acquire the spectrum correctly, photoelectrons must reach the detector without collisions with other molecules, therefore ultrahigh vacuum is required. Such conditions can be fulfilled for non-volatile

solid surfaces and diluted gaseous samples, where PE spectroscopy has become a common analytical tool.

To study volatile samples, one needs to ensure that the transfer of electrons to the detector is essentially collision-free despite a relatively high vapor pressure, which became possible recently thanks to the vacuum liquid microjet technique [19]. If the diameter of the liquid jet is of the order of 10 μm , gas-phase water density decreases quickly in the radial directions such that the electron transfer-length increases to the 1 mm range [51]. The problem of evaporative cooling of high-vapor-pressure liquids in vacuum is solved by the fast flow of the liquid which also eliminates aging effects on the sample. The source of photons can be synchrotron radiation in case of soft X-ray experiments or laser pulses for ultraviolet and extreme ultraviolet light.

While kinetic energy measurements are more or less straightforward, the quantitative analysis of PE signals is rather complicated. The dependence of the electron intensity on the depth from the surface is empirically known to show an exponential attenuation [52], so the actual signal measured in the experiment is the integrated intensity over the exponential attenuation length into the solution [51]. The dependence of the electron signal on detection angle is not well known especially at the surface, but first attempts towards its understanding have been made already [53]. Other complications arise in multicomponent solutions, because reliable photoionization cross sections for solutes are hardly available. Due to all these uncertainties, it has become a common practice to calibrate solute valence energies with respect to the water $1b_1$ energy (11.16 eV) and core-level spectra to the water O1s energy (538.1 eV) for experimental assignment of the solute ionization energies. The PE spectrum of the investigated aqueous species is obtained as a difference between the spectra of its solution (water + buffer + investigated species) and exactly the same solution without the given solute (water + buffer).

Chapter 3

Improving force fields for concentrated salt solutions

Accurate description of concentrated salt solutions employing classical MD simulations with empirical force fields remains a non-trivial task, because the majority of models were parametrized using measurable quantities of a single ion at infinite dilution. Therefore, it is not clear, how such models capture the ion-ion interactions which play an important role in concentrated solutions. Nevertheless, investigating concentrated solutions is advantageous both from the experimental point of view due to the stronger ionic signal and in simulations, where direct sampling is sufficient because the presence of various pairs in different arrangements speeds up convergence of the structural characteristics. The first section of this chapter presents results for aqueous salt solutions of lithium with monovalent and divalent anions, namely Cl^- and SO_4^{2-} . The second section discusses applicability of effective accounting for polarization in inhomogeneous systems possessing the air/water or the oil/water interface. All calculations in this chapter were performed with the Gromacs 4 program package [54].

3.1 Ion pairing in lithium salt solutions

Lithium has many important practical applications, such as Li-ion polymer batteries [55] or lithium carbonate in the glass and porcelain industries. Li^+ in aqueous solutions is also interesting from the physical chemistry point of view, because it has the highest charge density among the alkali metal ions, which affects the surrounding water molecules. The Li^+ hydration structure deduced from earlier experiments [6, 56–58] is not reproduced by standard non-polarizable FFs [58–60]. In order

to get a better description of the molecular structure of lithium aqueous solutions, we compare recent neutron scattering results [61] with MD simulations where we employ the ECC approach, i.e., rescaling the ionic charges, introduced in section 2.3, and also further refining of the ionic radii [62] (attached as the 1st publication).

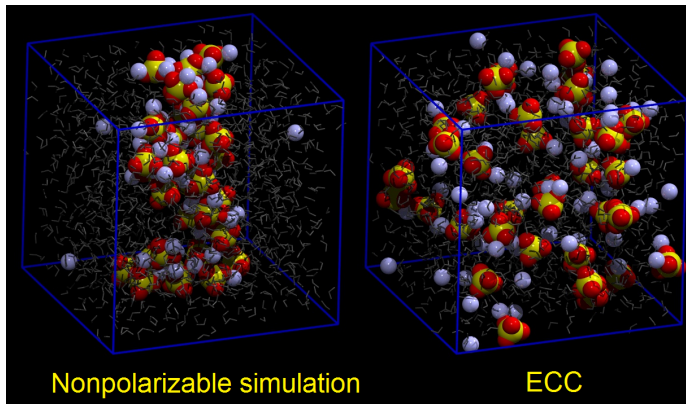


Figure 3.1. Snapshots from simulations of a 1.5M Li_2SO_4 solution with a non-polarizable force field (left), where the ions strongly aggregate, and with ECC charges (right), where the ions are more homogeneously distributed. Water molecules are shown in stick representation.

The simulation box containing the 1.5 M Li_2SO_4 solution is depicted in Fig 3.1. In non-polarizable simulations with integer (full) ionic charges, ions cluster together regardless of the FF [62]. Such precipitation from the solution is in disagreement with experimental solubility of ~ 3 M. Effective inclusion of polarization restores the large solubility as is illustrated in Fig. 3.1 (right). The first step of quantitative characterization of the investigated solution is to evaluate the radial distribution functions (Eq. 2.3) as shown in Fig. 3.2 for the Li^+ ion. The first maximum of the Li^+ –oxygen (both water and sulfate) $g(r)$ is located at 2.1 Å, followed by a peak at 2.6 Å due to the hydrogen atoms of the water molecules in the first solvent shell of the ion. The arrangement of Li^+ and SO_4^{2-} can be bidentate, which corresponds to the small shoulder at 2.9 Å of the $g_{\text{LiS}}(r)$, or monodentate, corresponding to the larger peak at 3.4 Å.

Using the scattering factors for the solution containing ^6Li and ^7Li isotopes in Eq. 2.9, we evaluated the difference $G(r)^{(^6\text{Li})} - G(r)^{(^7\text{Li})}$ for simulations performed with two lithium van der Waals sizes and full or ECC ionic charges. These theoretical predictions together with experimental results are plotted in Fig. 3.3. As discussed above (Fig. 3.2), the peak at ~ 2 Å is due to the oxygen atoms solvating the ion, and the peak at 2.6 Å due to the hydrogen atoms on the water molecules solvating the ion. If the lithium ion was surrounded only by sulfate ions, the second peak would

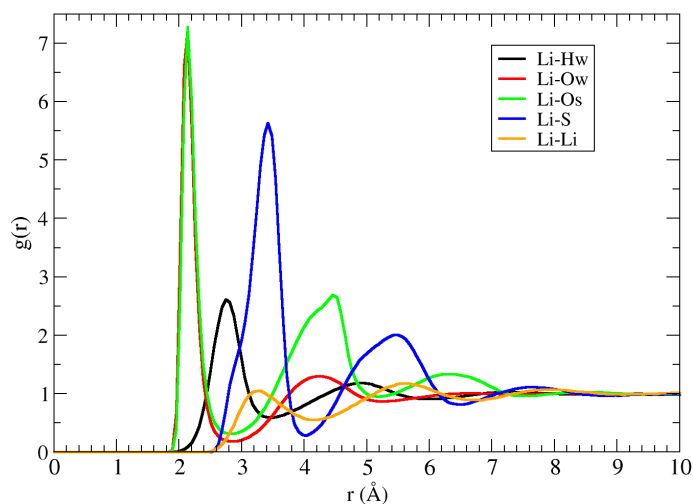


Figure 3.2. Radial distribution functions of Li^+ to water hydrogen (black), water oxygen (red), sulfate oxygen (green), sulfur (blue), and Li^+ (orange) in a 1.5M Li_2SO_4 aqueous solution modeled using the OPLS Li^+ with ECC ionic charges.

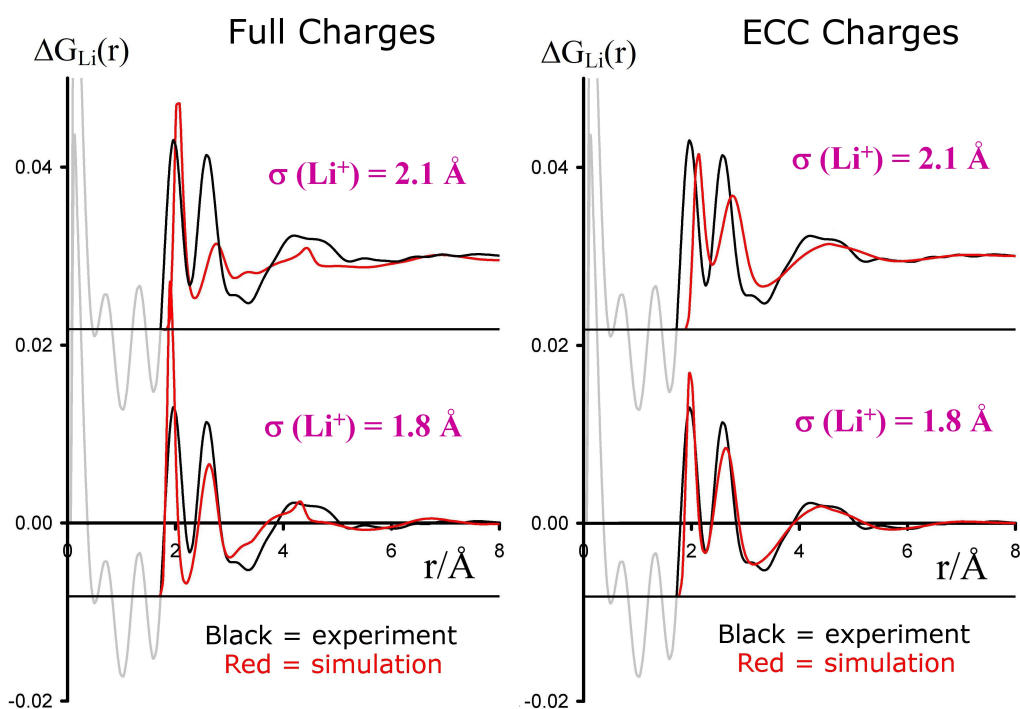


Figure 3.3. Structural characteristics $\Delta G_{\text{Li}}(r)$ of a 1.5 M Li_2SO_4 aqueous solution obtained from MD simulations (red) with two Li^+ ionic sizes (larger - top, smaller - bottom) and full (right) or ECC (left) ionic charges in comparison to experiment (black).

not be present. Therefore, the degree of ion pairing is related to the ratio of the size of the peaks, which is overestimated in both simulations involving full ionic charges, but is much closer to experiment for ECC. Prediction of the peak positions using the of-the-shelf OPLS parameters ($\sigma = 2.1 \text{ \AA}$) [63] is shifted towards larger distances in comparison to experiment, which has been generally observed in classical MD studies [57, 59, 60]. The smaller lithium radius ($\sigma = 1.8 \text{ \AA}$) was chosen based on the assumption that a linear reduction in the radius would lead to a linear shift in the peak position. Reparametrization of the lithium ion together with ECC provides a good fit to the experimental data (Fig. 3.3 right, bottom).

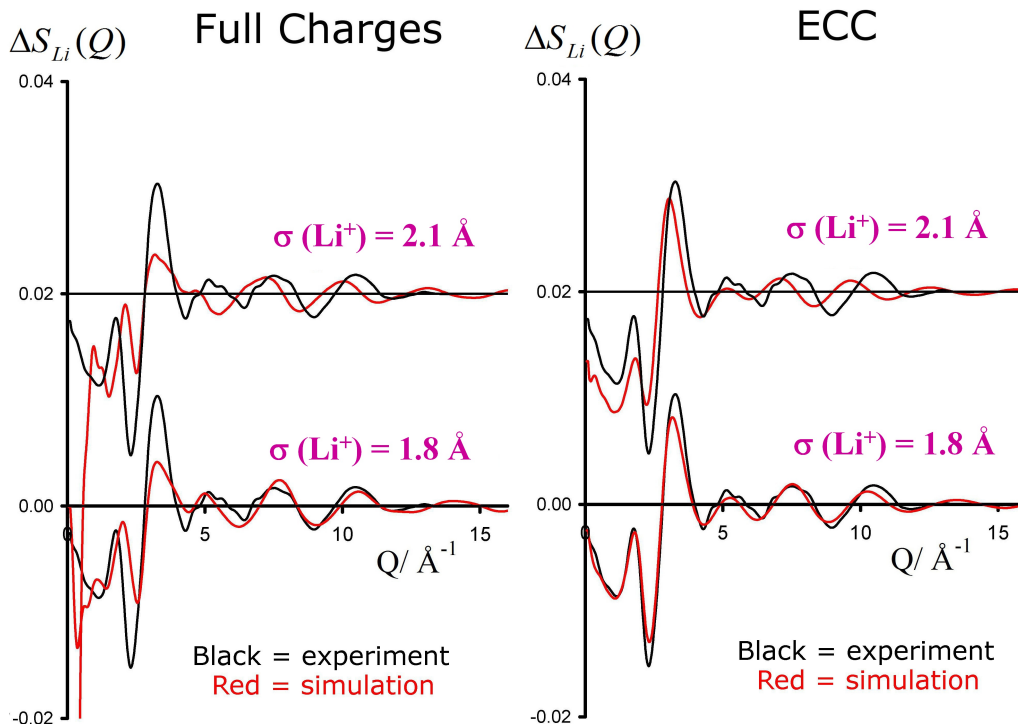


Figure 3.4. First order difference of structure factors $\Delta S_{Li}(Q)$ of a 1.5 M Li_2SO_4 aqueous solution obtained from MD simulation with two Li^+ parametrizations (larger - top, smaller - bottom) and full (right) or ECC (left) ionic charges with comparison to experiment (black).

The previous paragraph compared simulated and experimental data in the r -space, which is a more intuitive method of visualization. However, the Q -space representation should be also considered, because it is closely related to what is directly measured in the experiment. Both comparisons in principle contain exactly the same amount of information, however they emphasize different aspects of the structure. $S(Q)$ is back Fourier transformed from $G(r)$, hence sharper features at lower r correspond to longer wavelength features in Q . The first two peaks at r of about 2

and 2.6 Å effectively produce two sine-type waves of different frequencies in the Q -space. The fact that the positions of the two peaks do not match the original lithium parametrization, even though the difference of ~ 0.1 Å seems small, causes a notable phase shift in the data at higher Q in the Q -space. The longer range features in the r -space, roughly past the first hydration shell, correspond to high frequency elements in the Q -space. This is demonstrated in Fig. 3.4, where the simulations with full ionic charges, having more longer range structure, show an incorrect signal in the lower Q region, which is corrected employing ECC.

Next, we compare ion pairing of lithium with a divalent anion, described above, with the most common monovalent aqueous anion Cl^- . We again use the same four types of force fields for ions: OPLS [63] and reparametrized Li^+ ($\sigma = 1.8$ Å), both with or without using the ECC approach. All collected trajectories of the 3 M LiCl solution exhibit regular behavior, i.e., no excessive ion pairing. We observed analogous, but less pronounced changes as in the lithium sulfate case when comparing structural characteristics obtained employing the above mentioned FFs, i.e., less ion pairing in the ECC simulation and good agreement of the peak positions of $\Delta G_{\text{Li}}(r)$ for reparametrized Li^+ ($\sigma = 1.8$ Å). To conclude this lithium study, for both investigated solutions the electronic continuum correction together with reparametrized, i.e., smaller Li^+ gives a good agreement with experimental neutron scattering data and simulations provide their interpretation in full atomistic detail.

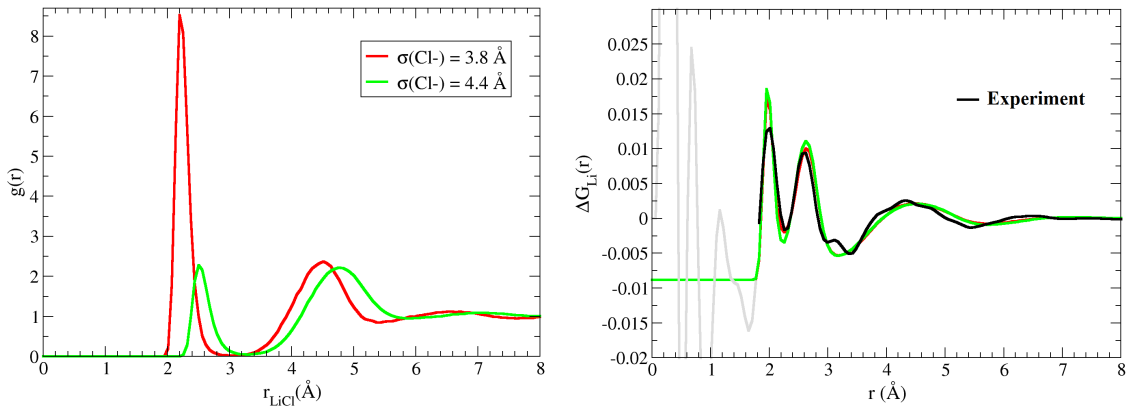


Figure 3.5. The Li–Cl radial distribution function in a 3M LiCl aqueous solution simulated employing Dang (red) and OPLS (green) parametrization of Cl^- with the ECC ionic charges (left). Comparison of calculated $\Delta G_{\text{Li}}(r)$ for both FFs to experiment (black) (right).

Despite the prevalence of Cl^- , there exist only a handful of studies comparing the structure of its concentrated solutions predicted by MD to the structural measurements [6, 9, 57, 65–68], and comparison to NDIS is even rarer [69]. First, we checked

the influence of chloride parametrization on the Li^+ structural characteristics in the 3M LiCl solution by comparing the following frequently used parametrizations: OPLS ($\sigma = 4.4 \text{ \AA}$) [63] and Dang ($\sigma = 3.8 \text{ \AA}$) [64] Cl^- using the ECC approach. Fig. 3.5 shows the $\text{Li}-\text{Cl}$ radial distribution functions, which demonstrates that the peak positions and heights are indeed dependent on the parametrization. However the simulated $\Delta G_{\text{Li}}(r)$ almost coincide with each other, so this structural function does not contain considerable amount of information about Cl^- except for ion pairing which is related to the number of water molecules in the vicinity of Li^+ .

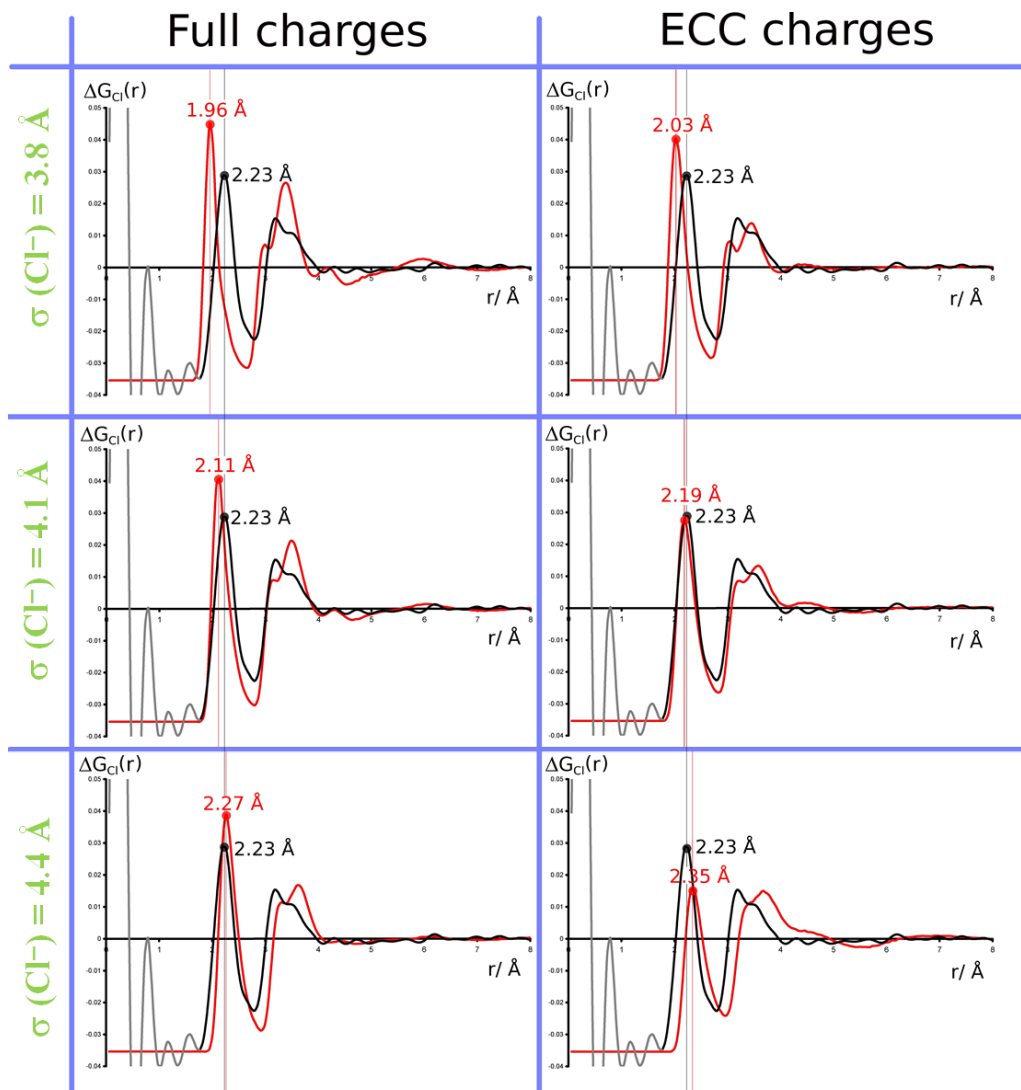


Figure 3.6. $\Delta G_{\text{Cl}}(r)$ in a 6m LiCl aqueous solution calculated using three chloride parametrization without and with ECC approach (red) and compared to the experimental data (black).

It was, therefore, necessary to perform NDIS measurement with isotopically sub-

stituted chloride in more concentrated (6m) LiCl solution, which is required due to the lower absorbance of neutrons by both ^{35}Cl and ^{37}Cl isotopes in comparison with ^6Li [70] (attached as the **2nd** publication). The structural characteristics $\Delta G_{\text{Cl}}(r)$ of this solution obtained from experimental measurements and simulations employing different FFs are plotted in Fig. 3.6. The position of the first peak, which corresponds to one of the water hydrogens pointing towards Cl^- , is sensitive to the anionic size. Since the predictions by the two common FFs mentioned above with ECC do not match the experiment, we made a refinement, yielding a medium sized chloride ($\sigma = 4.1 \text{ \AA}$) giving the first peak in the $\Delta G_{\text{Cl}}(r)$ coinciding with measurement. The signature of the remaining atoms of the water molecules in the first solvent shell, i.e., oxygen and the second hydrogen, is the partially resolved doublet at 3.5 \AA . MD simulations predict a slightly larger peak for hydrogen than for oxygen regardless of the FF, while the experiment shows the opposite. Only the simulation employing the medium-sized chloride with the ECC charge accurately reproduces both the first and the second peak in $\Delta G_{\text{Cl}}(r)$. Reproducing the shape of the $\Delta G_{\text{Cl}}(r)$ in the region of the second hydration shell is much more difficult, because relatively minor changes in the three-dimensional structure of the aqueous solution can lead to significant differences in this function. Thus, the influence of the water model also comes into play [70].

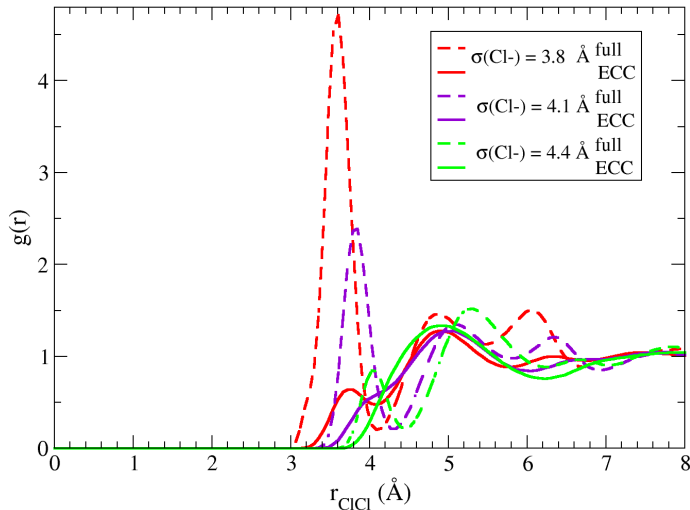


Figure 3.7. Cl-Cl radial distribution functions in a 6m LiCl aqueous solution calculated with full (dashed line) or ECC (solid line) ionic charges and three chloride parametrizations (red, purple, and green ordered according to the increasing size of the ion).

Finally, we present the most force field dependent radial distribution function,

which is the one for the like-charged ions. The smallest and the medium-size full charge Cl^- exhibit pronounced contact maximum (Fig. 3.7) while the others do not. For separations larger than $\sim 5 \text{ \AA}$, the $g(r)$ just slightly oscillates around one. Since the contribution of the $g_{\text{ClCl}}(r)$ to the $\Delta G_{\text{Cl}}(r)$ is small, our current experimental data cannot resolve the old discussion about pairing of simple like-charged ions in water [71], nevertheless, our best force field points to a very weak effect (if any).

3.2 Aqueous interfaces

In the previous section we showed that ECC provides an improvement in theoretical modeling of the structure of concentrated aqueous electrolytes in comparison with non-polarizable simulations. Another research topic, where including polarizability is also important, is the affinity of soft inorganic ions (such as iodide, bromide, thiocyanate, etc.) to the air/water interface. The forces driving them to the interface are complex, but an important one originates from the ability of water molecules to polarize the ion and vice versa [72]. Therefore, it seems worth trying to use the computationally cheaper ECC instead of fully polarizable simulations. However, the ECC approach is not theoretically justified for systems with discontinuity in electronic polarization properties. Nevertheless, a previous study of iodide with charge set to $-0.75 - -0.8$ without any theoretical justification found enhanced affinity to the air/water interface in comparison with the non-polarizable simulation [73].

We systematically explored behavior of sodium halides (F^- , Cl^- , Br^- , and I^-) with full and ECC ionic charges in a water slab, i.e., at the air/aqueous solution interface. Next, in order to get rid of the discontinuity in the ϵ_{el} , which is not consistent with the ECC approach, we modeled the aqueous solution/decane interface [74] (attached as the 3rd publication) as is illustrated in Fig. 3.8, where the values of ϵ_{el} of the two media are almost the same [31, 75].

The effect of charge scaling and presence of solution/decane instead of solution/air interface is demonstrated in Fig. 3.9 which shows Cl^- density profiles, i.e., averaged densities from collected trajectories along the normal to the interface. In both simulations with full ionic charges (Fig. 3.9 a, c), chloride is repelled from the interface, which leads to a negative net interfacial excess of ions. In the ECC simulations Cl^- exhibits an interfacial peak, which is larger at the solution/air interface than at the solution/decane interface, followed by a depletion zone just below the interface. The counter-ion, i.e., sodium exhibits a peak in the anion depletion zone. The net interfacial excess of ions is slightly positive for the former and zero for the

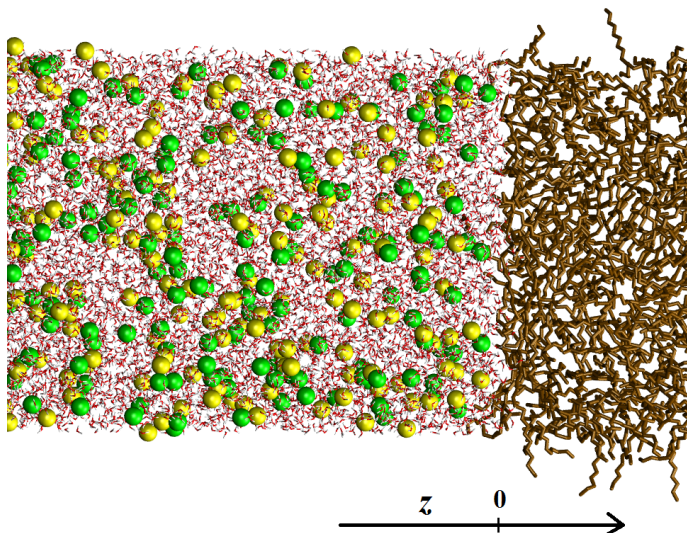


Figure 3.8. A snapshot of the part of the system containing 1M NaCl aqueous solution with the aqueous solution/decane interface. Cl^- is represented by yellow spheres, Na^+ by green spheres, united atom decane by brown sticks, and water molecules in line representation. The arrow of the z -axis indicates how density profiles in Fig. 3.9 are plotted.

later ECC simulation.

To summarize results for other halides at the solution/decane interface, all non-polarizable simulations show a negative net interfacial excess of ions unlike the experiment [76]. The surface propensities of the anions for the solution/decane interface in the ECC simulation increase in the order $\text{F}^- < \text{Cl}^- < \text{Br}^- < \text{I}^-$, with the interfacial excess being negative for F^- , around zero for Cl^- and Br^- , and positive for I^- . Semi-quantitatively, the simulation predictions agree with earlier measurements showing that iodide unlike lighter halides behaves as a weak surfactant at the solution/oil interface [74, 76]. The solution/air interface exhibits a sharp discontinuity in the ϵ_{el} dropping from 1.78 to 1, therefore, the ECC ionic charges are “overscaled” at the interface as if the ϵ_{el} was the same in air and water. This leads to an overestimation of the affinity of anions to the interface which is manifested by a positive ionic interfacial excess for halides heavier than fluoride. Thus, the simple and computationally inexpensive effective account for polarization provides a reasonable description for aqueous interfaces with hydrophobic liquids, but reaches limits of its validity in case of the solution/air interface.

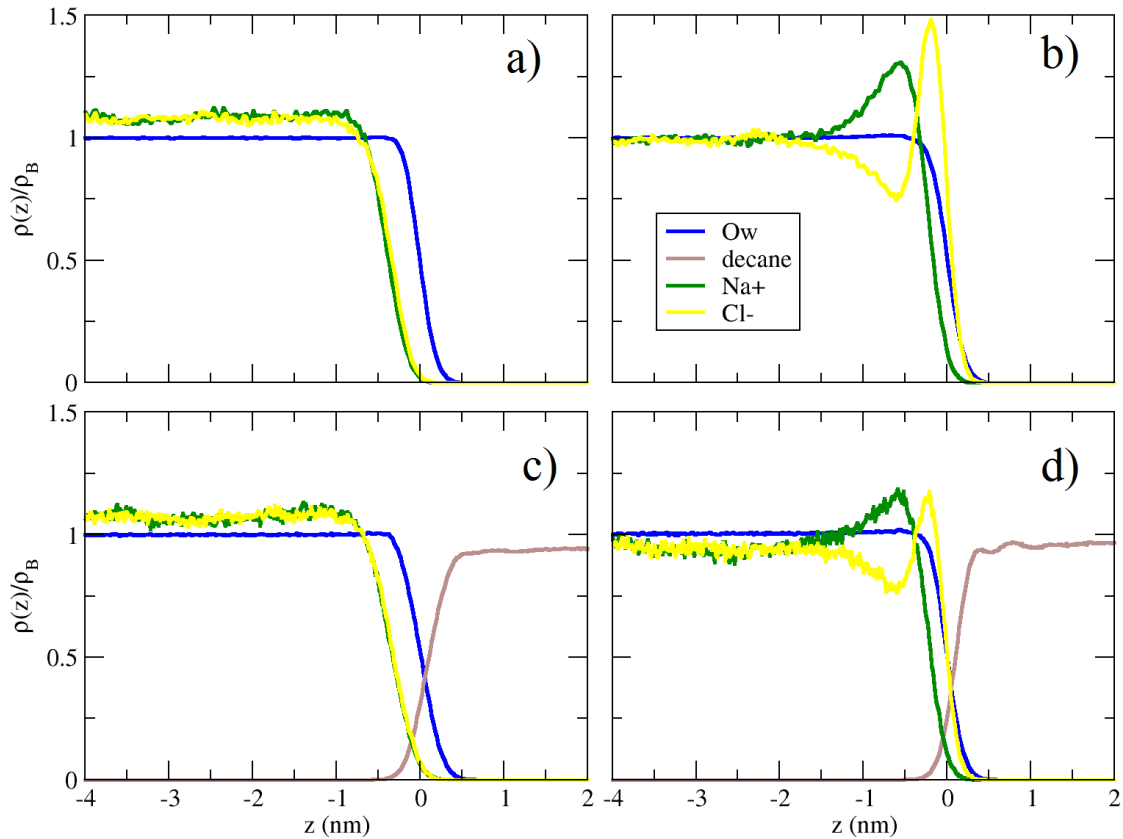


Figure 3.9. Symmetrized number density profiles $\rho(z)$ of water oxygen (blue), decane (brown), sodium (green), and chloride (yellow) plotted vs. z , i.e., the normal to the interface, normalized by the bulk density of water ρ_B with ion densities scaled by the water/ion concentration ratio of 55.56. a) solution/air interface with full ionic charges, b) solution/air interface with ECC ionic charges, c) solution/decane interface with full ionic charges, and d) solution/decane interface with ECC ionic charges.

To summarize, we showed in this chapter that empirical force fields with careful parametrization can provide valuable information about aqueous solutions and interfaces with atomistic resolution. However, every empirical parametrization reaches its limits of validity at some point, in which case we opt for non-empirical *ab initio* MD as described in the next chapter.

Chapter 4

Ion pairing by *ab initio* molecular dynamics

Understanding ion pairing and specific ion effects on proteins in aqueous solutions remains a considerable challenge. To address the issues of ion–ion and ion–peptide bond interaction in water we use in this chapter *ab initio* MD simulations. In comparison with empirical forces fields, these have several advantages, e.g., less parameters, possibility of bond breaking and formation, or modeling infrared spectra without empirical fitting, but they can be prohibitively expensive. Due to the computational cost and also slowed down sampling due to the smaller number of pairs free energy methods have to be frequently utilized instead of direct sampling. All DFT-based BOMD simulations were performed with the CP2K program package [33] with the following important ingredients - the TZV2P MOLOPT basis set [77], the GTH pseudopotential [34], and the BLYP functional [78, 79] with the empirical Grimme dispersion correction [80].

As our first example we have chosen a geometrically simple, but electronically non-trivial case of lithium fluoride in bulk water. The next step is the investigation of the strength of the interaction of calcium and sodium cations with N-methylacetamide (NMA), which is one of the simplest molecules containing the peptide bond. Therefore, it can serve as a suitable model for studying interactions at the protein backbone. Finally, we explored behavior of a model dipeptide containing both the peptide backbone and charged side chains termini upon sequential addition of water molecules.

4.1 LiF ion pair

The aim of this section is to present a reliable computational protocol for evaluating the free energy profile for the ion–ion dissociation by combining the DFT based BOMD with the potential of mean force calculations and, on top of that, analyze the electron density [81] (attached as the 4th publication). Fig. 4.1 shows the investigated system consisting of one LiF ion pair in a box of 64 water molecules, which is large enough not to cause significant artifacts due to the system size [81–83]. Before starting a series of extensive BOMD simulations with the LiF distance constrained to different values (section 2.1), we carefully explored the statistical and systematic uncertainties. The first one is related to the duration of the simulation and we estimated it from classical MD simulation with an empirical force field, where we collected long trajectories (tens of ns). These were divided into blocks of different length for each of which we evaluated the mean force and then performed averaging over the blocks to get the standard deviation as a function of the simulation length. The resulting dependencies for four different ion–ion separations are plotted in the right part of Fig. 4.1. Based on that we decided to collect a 50 ps trajectory in each of the simulation windows.

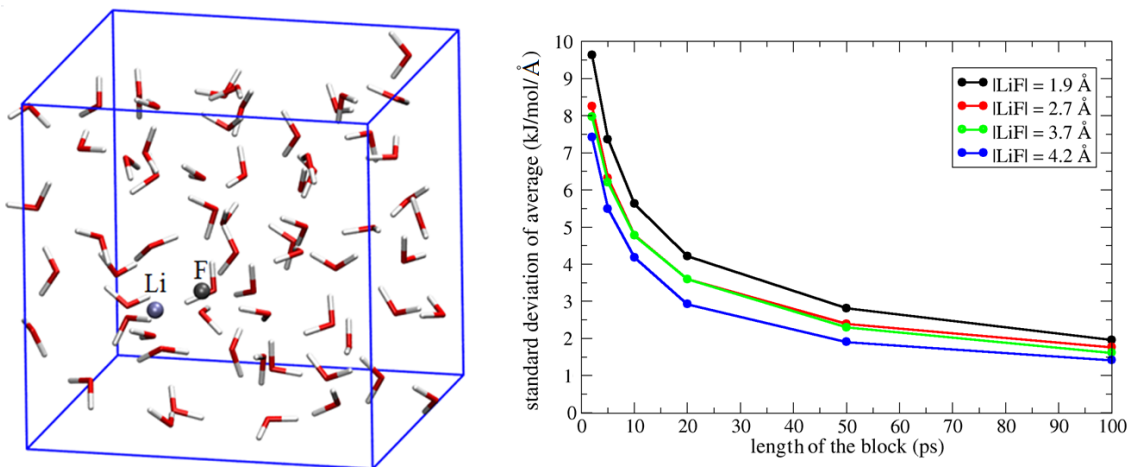


Figure 4.1. Snapshot of the investigated system containing LiF and 64 water molecules in a 12.6 Å cubic box (left). Standard deviation of the mean force acting along the ion-ion distance for four lithium–fluoride separations calculated employing the OPLS/TIP4P empirical force field as a function of the duration of the simulation (right).

To estimate the systematic error is more difficult. One possibility is to compare the energies of clusters calculated using our BOMD setup with higher level *ab initio*

methods. The other way is to characterize hydration of ions in bulk solution by, e.g., radial distribution functions or coordination numbers and compare such properties with available experimental data. Both approaches provide a satisfactory agreement.

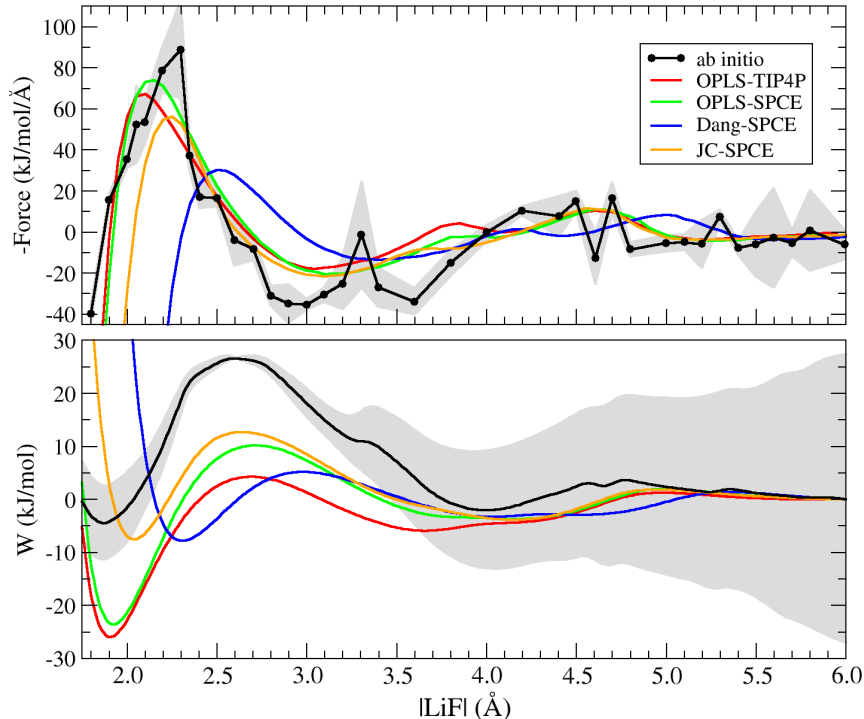


Figure 4.2. The mean force (upper part) and the potential of mean force (lower part) along the Li-F distance. BOMD mean forces (black circles) were calculated for 38 points corresponding to 50 ps trajectories after 5 ps of equilibration each. The grey area in the upper part corresponds to the statistical error in force evaluation estimated by the block average analysis method, which being integrated gives an upper bound to the error of the potential of mean force (grey area in the lower part). Comparison is made for the same system simulated using four different empirical force fields (colored lines). All free energy profiles are normalized to zero at the largest investigated ion-ion separation. Adapted from our publication [81].

After these checks, we evaluated the average force for each of the 38 AIMD trajectories (with constrained interionic distances) of 50 ps length as shown in the upper part of Fig. 4.2. For most points the standard deviation (grey area) is below the estimate from classical MD of ~ 4 $kJ/mol/\text{Å}$ (but occasionally it can exceed this value, as, e.g., for the point at 3.3 Å). The corresponding potential of mean force with the accumulated error during the integration procedure, which represents an upper bound, is displayed in the lower part of Fig. 4.2. The contact ion pair (CIP) is situated at 1.9 Å, with $\bar{F} = 0$ for the first time from the small distances side. The transition state lies at a Li-F distance of 2.6 Å about 30 kJ/mol above the CIP

(note that we chose to start the accumulation of the integration error here). The solvent shared ion pair (SIP) minimum is located at the ion–ion separation of 4.0 Å with a similar value of the free energy as for the CIP. For larger distances the PMF converges to zero, as expected. Both panels of Fig. 4.2 also present comparison with different empirical force fields [63,64,84], results of which vary considerably showing again the need for the *ab initio* based approach. The prediction of the positions of the CIP and SIP are FF-dependent, with OPLS reproducing best the position of the first one and the barrier height, but underestimating the depth of the SIP minimum.

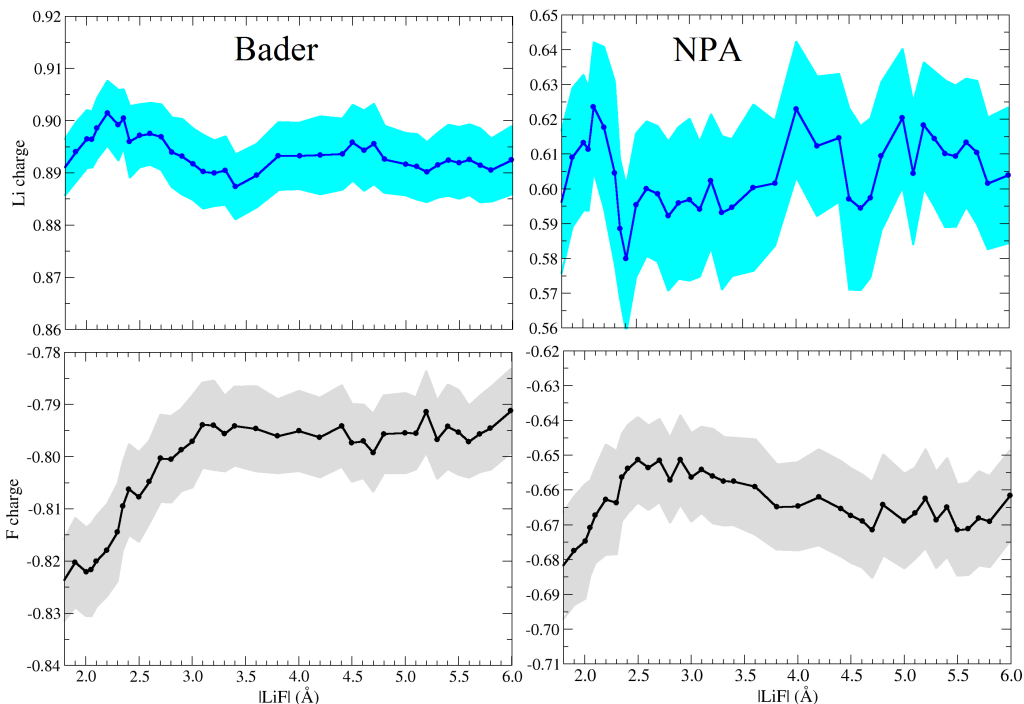


Figure 4.3. Bader charges (left) and NPA charges (right) of Li (blue) and F (black) as functions of the LiF separation. Solid lines with circles indicate the average values, while shaded areas depict regions within one standard deviation.

We can take advantage of having the electron density at hand and analyze it using the Bader population scheme [85] to assign the ionic charges. However, the partial charge is not a measurable quantity, so its value is definition dependent. To check for this we compare the Bader charges with the natural population analysis (NPA) [86]. Results of both population schemes are depicted in Fig. 4.3: Bader (left) and NPA (right). The lithium Bader charge does not depend appreciably on the Li–F separation, it varies between 0.89 to 0.90 |e|, but the fluoride Bader charge increases from -0.82 to -0.79 |e| upon dissociation of the CIP. The standard deviation of the

Bader charges is always below 0.01 |e|, while the NPA charges fluctuate at least twice as much and their absolute values are smaller. The lithium NPA charge oscillates from 0.58 to 0.62 |e|, while the fluoride NPA charge increases from -0.68 to -0.65 |e| upon the CIP dissociation and then slightly decreases again. Both analyses indicate that there is a non-negligible amount of charge transferred from ions to the solvent and show a similar trend upon the ion pair dissociation, but the exact values of partial charges should be used with caution.

To sum up, we presented our successful attempt to evaluate the free energy profile for the LiF ion pair dissociation by the BOMD simulations with the potential of mean force method and addressed the issue of charge transfer from ions to solvent. Water not only creates an “environment” for the ions and affects their electronic structure, but also significantly influences the kinetics of the ion pair dissociation. Deeper understanding of this problem by comparing the widely used Grote-Hynes theory and reactive flux trajectories is under way. In the future, the established computational protocol will allow us to investigate biologically more interesting ion pairs such as Ca^{2+} with formate as a proxy of acidic amino acid side chains.

4.2 N-methylacetamide with cations

More than one hundred years after Hofmeister’s pioneering work, there are still unresolved issues concerning the interaction of the peptide bond with ions. For example, there is a debate about alkali and alkaline earth cations, where partitioning models predict substantial binding of Ca^{2+} , Li^+ , or Na^+ with the backbone [87], classical MD simulations with empirical FF indicate at least some binding of Na^+ [88,89], but the recent amide I IR measurements deduced a very weak (actually none for Na^+) cationic interactions [90]. To obtain a deeper insight into this problem we investigated the interaction of Na^+ and Ca^{2+} with NMA in bulk water by combining free energy calculations and IR spectra predictions from the DFT based BOMD simulations [91] (attached as the 5th publication).

For a first estimate of the structure of NMA in neat water and with Ca^{2+} and Na^+ bound to the carbonyl oxygen, we ran direct 50 ps simulations, in which both ions remained in a contact arrangement for the duration of the simulation. The C=O group in neat water binds two, sometimes even three water molecules. Sodium replaces one water molecule, and it exhibits a tilted arrangement with respect to the C=O axis with a mean $\text{O}\cdots\text{Na}^+$ distance of 2.4 Å. Calcium stayed bound at a similar distance, i.e., between 2.3–2.4 Å with a narrower distribution of the distances

indicating stronger attraction. Moreover, Ca^{2+} prefers binding in a collinear fashion with no additional water molecule bond to the carbonyl group most of the time. These observations are visualized by density maps in the right panel of Fig. 4.4.

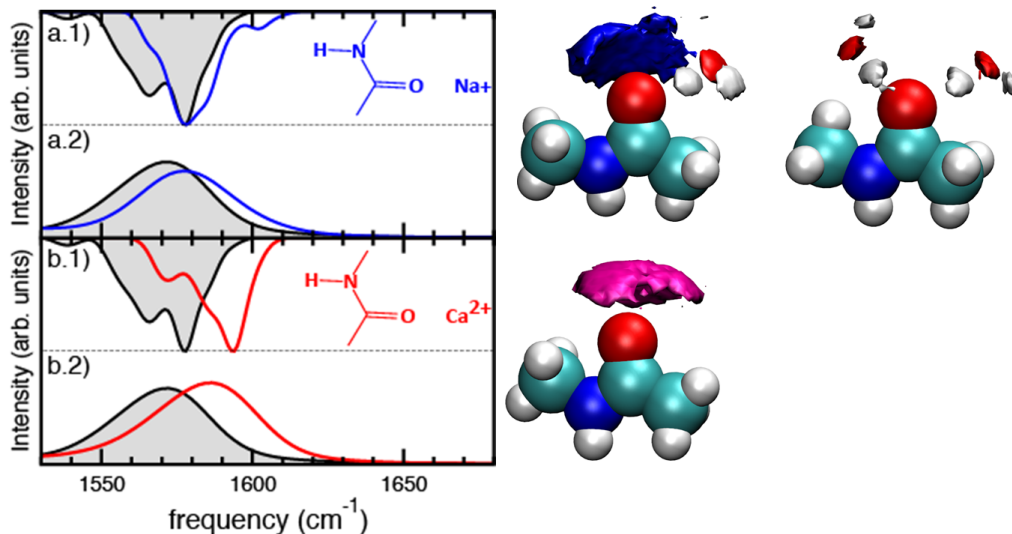


Figure 4.4. Left panel: comparison of the ensemble averaged C=O bond length power spectrum of NMA in neat water (grey with black outline, a.1 and b.1), in contact with Na^+ (blue, a.1), and in contact with Ca^{2+} (red, b.1). The IR-absorption spectra based on the autocorrelation of the molecular dipole are shown in a.2) and b.2) for free NMA, in a.2 for NMA in contact with Na^+ , and in b.2 for NMA in contact with Ca^{2+} . Right panel: density maps of Na^+ (blue), Ca^{2+} (magenta), and water oxygen (red) and hydrogen (white) around the carbonyl group of aqueous NMA.

How do these structural patterns exhibit themselves in experimentally measurable quantities? We calculated the carbonyl stretch frequency within the amide-I band of the free NMA and NMA with the cation bound in deuterated bulk water using either the power spectra of the C=O bond length or the maximally localized Wannier functions for evaluation of the dipole moment [92–94]. The simulated spectrum of the ion-free aqueous NMA has a broad peak around 1570 cm^{-1} as shown by black line in the left panel of Fig. 4.4. The presence of Na^+ does not shift the absorption spectrum significantly (blue curve in Fig. 4.4), unlike Ca^{2+} which causes a blue shift of about 23 cm^{-1} which agrees well with the experimentally observed spectra [90]. Based on the predicted spectra, the IR measurement is sensitive to the formation of the contact pair between calcium and the carbonyl group, but it can not detect the proximity of Na^+ .

We have shown above that both cations can stay in contact with the peptide bond, but to estimate the binding strength, additional umbrella sampling simulations

are necessary. In principle, three variables are needed to describe the position of the cation with respect to the NMA molecule: the O \cdots ion distance, the C-O-ion angle, and the deviation from the peptide bond plane. However, sampling of the whole distribution within the BOMD simulations is not feasible. Nevertheless, we at least checked the influence of limited angular sampling on the free energy profile as a function of the O \cdots ion distance by the computationally much less demanding classical MD with empirical FF. The effect luckily turned out to be minor [91]. Umbrella sampling windows along the O \cdots ion distance varying from 2.5 to 6.5 Å were equally spaced by 0.5 Å with additional windows at the barrier region to ensure dense enough sampling. In each of the windows we ran a 50ps BOMD trajectory after at least 5 ps of equilibration.

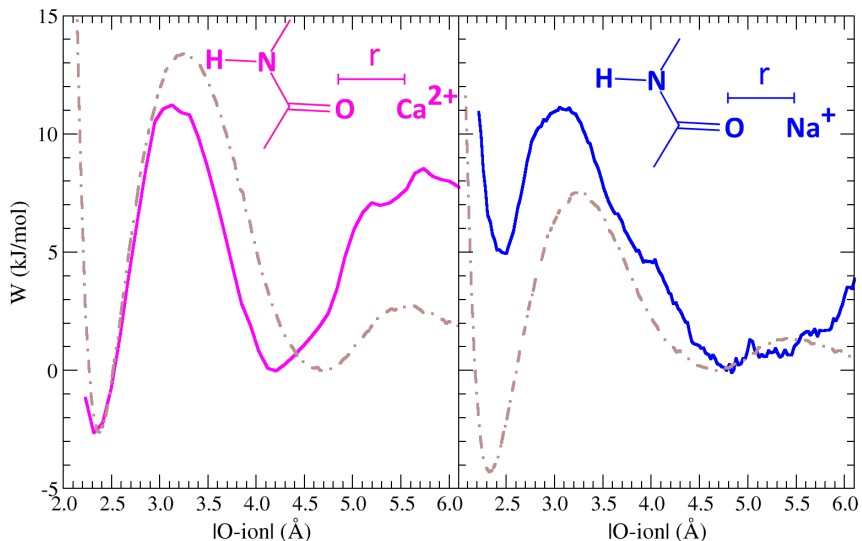


Figure 4.5. Free energy profiles for the CO \cdots cation dissociation obtained by umbrella sampling with BOMD (colored full lines) or force field MD (brown dot-dashed lines). The free energy of the solvent shared state is set as zero in all cases. All profiles are corrected by the volume entropy factor of $2 \cdot k_B T \ln(r/r_0)$. Adopted from our publication [91].

The BOMD free energy profiles for the C=O \cdots Ca $^{2+}$ and C=O \cdots Na $^{+}$ interactions are plotted in Fig. 4.5. The contact pair minimum for calcium is situated at 2.35 Å, the transition state lies about 14 kJ/mol above it at the separation of 3.1 Å, and the solvent shared minimum is located at 4.2 Å about 3 kJ/mol above the contact structure. The relative energetic positions of the two minima for sodium differ from those for calcium, i.e., the contact structure for sodium at 2.4 Å represents the shallower minimum lying ~ 5 kJ/mol above the deeper solvent shared structure situated at 4.8 Å. The barrier height with respect to this lower minimum is about 12

kJ/mol. Judging from the shape of the converged free energy profiles from empirical FFs, the free energy profile should not change much for separations larger than 6 Å, but it is difficult to accurately assign the relative stability of the described minima with respect to infinite separation due to the limited sampling in the BOMD simulations. Nevertheless, the present *ab initio* MD simulations show that both Ca^{2+} and Na^+ interact with NMA, but differ in their affinities, the arrangement in the contact structures, and the spectroscopic signatures.

4.3 Dipeptide salt bridge

This section presents results from our study of the salt bridge stability for a capped lysine-glutamate (Ac-Lys-Glu-NHMe) dipeptide under different degrees of hydration [95] (attached as the 6th publication). It is interesting and topical to investigate how interactions between acidic and basic side chains change as one adds water molecules, moving from the situation pertinent to desolvated side chains (a proxy of buried salt bridges) to the aqueous bulk phase similar as at the outer protein surface. In the former case with a low effective dielectric constant the Coulomb attraction between the side chains is more pronounced and the salt bridge can become stronger, however, the possibility of a neutralizing proton transfer between the chains needs to be taken into account as well. The later case, where the two groups are fully exposed to water, corresponds to a weak salt bridge, because the Coulomb interaction between the charged residues is screened. Gradually adding solvent molecules allows for investigating the interplay between the following forms:

salt bridge neutralized by proton transfer \rightarrow *strong salt bridge* \rightarrow *weak salt bridge*.

First we explored balance between the first two forms, i.e., neutral and zwitterionic arrangement of the model dipeptide shown in Fig. 4.6 (left) with up to five water molecules by direct BOMD in order to allow for the proton hopping. The bare dipeptide prefers to be in its neutral state. If the simulation is started from a zwitterionic initial condition, the proton hops back on a sub-picosecond timescale, once the charged side chains get close enough to each other. Upon adding water molecules, a plethora of structural motifs emerges as shown in Fig. 4.6 (right). The contact neutral state (Fig. 4.6 a) is a typical arrangement for clusters with one or two water molecules. The solvent shared neutral state (Fig. 4.6 b) is also found to be stable for one or two water molecules on the time scale of our simulations (20 ps), probably because neutral side chain termini do not attract each other too strongly.

The zwitterionic form (Fig. 4.6 c) appears when a single water molecule is attached to the dipeptide, if additional stabilization from the backbone is provided. In this particular case, the charged residues are stabilized by two hydrogen bonds from the water molecule and one from the backbone. With two water molecules, we observe another zwitterionic arrangement which combines stabilization of the backbone and both water molecules between the amino group and one of the carboxylic oxygens (Fig. 4.6 d). With three water molecules, there are more possibilities for the salt bridge to stay zwitterionic on the time scale of our simulations and for four water molecules, the dipeptide is mainly found in this symmetrically solvated contact zwitterionic state. Already with two water molecules, one can plausibly think of a solvent shared zwitterion (Fig. 4.6 e, f), but this initial condition with such a small number of water molecules is not stable and within few ps it develops in the following two ways. Either the proton can be transferred through a water bridge from Lys to Glu or the charges come closer to each other to form a contact ion pair without sufficient stabilization by additional hydrogen bonds, therefore, the proton is further transferred to Glu. Conversion of such initial condition with three water molecules to the contact zwitterion is possible, because water molecules are able to find binding sites which provide sufficient stabilization. Already four water molecules promote a solvent shared pair formation from an initial contact ion pair, but such arrangement is short-lived and after less than 1 ps it flips back.

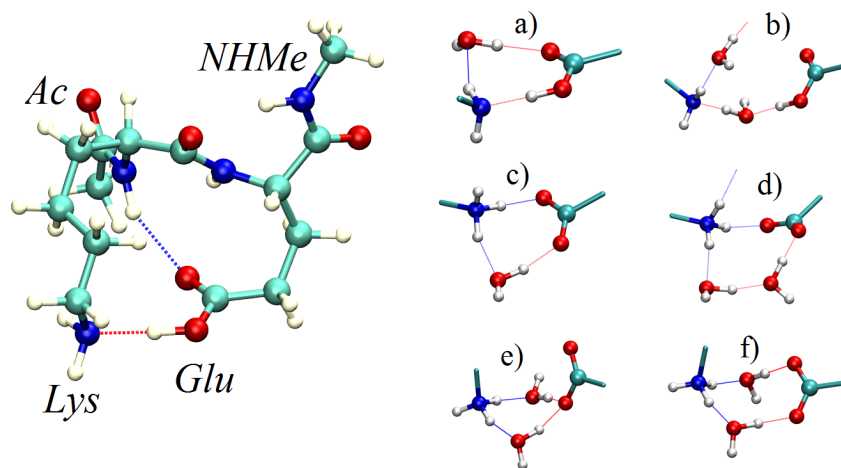


Figure 4.6. Group labeling of the Ac-Lys-Glu-NHMe model peptide (left) and details of the model peptide Ac-Lys-Glu-NHMe side chain termini (right). The dipeptide can be in neutral form with one water molecule (a) contact) and with two water molecules (b) solvent shared) attached, or in a zwitterionic contact pair with one (c) or two (d) water molecules attached, and solvent shared ion pairs involving one (e) or two (f) oxygen atoms of the carboxyl group.

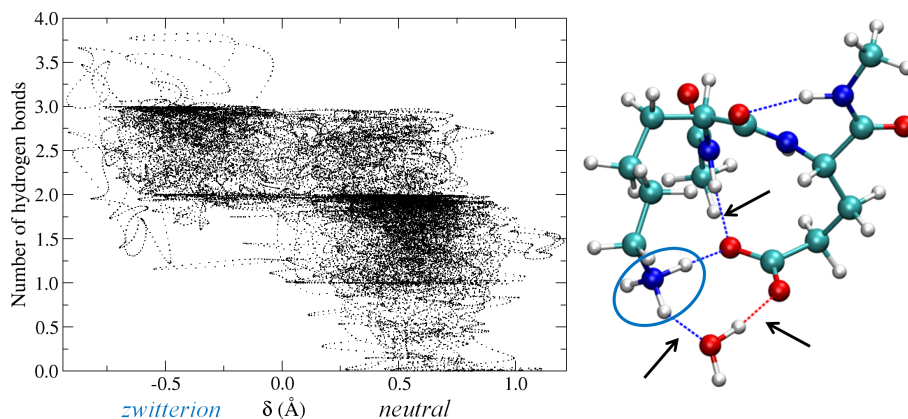


Figure 4.7. A smeared number of hydrogen bonds additionally stabilizing the side chain termini plotted against the proton asymmetry coordinate $\delta = r_{\text{NH}} - r_{\text{OH}}$ (left). The additional hydrogen bonds are marked by arrows (right).

From the case studies mentioned above, we can extract general conditions under which a proton can be transferred. The first one is a proper arrangement of the heavy atoms between which the proton hops. For a direct proton transfer between Lys and Glu, the NO distance must be smaller than 2.65 \AA while for a transfer through a bridge of a single water molecule the corresponding N-O(water) distance must be less than 2.55 \AA and the O(water)-O distance even below 2.45 \AA . Another important descriptor is the number of additional hydrogen bonds, meaning those in which the side chain termini are directly involved, but not the hydrogen bond between the amino and the carboxylic groups in contact arrangement (Fig. 4.7 right), or those involving a water molecule which serves as a bridge in the solvent shared arrangement. To visualize the relation, we used the asymmetry variable $\delta = r_{\text{NH}} - r_{\text{OH}}$ indicating whether the system is neutral ($\delta > 0$) or zwitterionic ($\delta < 0$) and smeared non-integer number of hydrogen bonds to avoid discrete jumps. For the donor-acceptor distance (r) and angle (α) we employed the following formula:

$$N_{HB} = 0.25 \operatorname{erfc} \left(\frac{r - r_0}{\sqrt{2}\sigma_r} \right) \operatorname{erfc} \left(\frac{\alpha - \alpha_0}{\sqrt{2}\sigma_\alpha} \right), \quad (4.1)$$

where $r_0 = 3.5 \text{ \AA}$, $\sigma_r = 0.25 \text{ \AA}$, $\alpha_0 = 30^\circ$, and $\sigma_\alpha = 5^\circ$. The correlation between the number of hydrogen bonds and δ is plotted in the left panel of Fig. 4.7. The neutral form exists for two or less hydrogen bonds. If the number of hydrogen bonds is between two and three, there is a dynamical equilibrium between the neutral and the zwitterionic state. Finally, for three and more additional H-bonds, the zwitterion is stabilized.

For clusters containing about 10 water molecules, the zwitterionic state without any proton transfer can be safely assumed to be stable, which allows for switching to the computationally less demanding empirical force field and much larger clusters and finally to the aqueous bulk where the interplay between contact, solvent shared, and solvent separated ion pair takes place. In order to simulate clusters with up to 1000 water molecules at room temperature and avoid evaporation, we harmonically restrain each of the water molecules to an immobile dummy atom with zero mass and no interaction parameters. To ensure more symmetric solvation of the side chains, also the midpoint between the charged side chain termini is restrained to this dummy atom. To disentangle the effect of the backbone and the aliphatic parts of the side chains on the salt bridge opening, we additionally simulated a simple $\text{NH}_4^+ \cdots \text{HCOO}^-$ ion pair.

The free energy profiles for the ion pair dissociation in water clusters of varying size were calculated using umbrella sampling. The free energy difference between contact and solvent shared $\text{NH}_4^+ \cdots \text{HCOO}^-$ ion pairs, as well as the barrier between them, decrease monotonically with the number of water molecules added, as shown in the right panel of Fig. 4.8. This is primarily caused by increasing dielectric screening of the charges. The bulk values of the barrier height (10 kJ/mol) and difference between the two minima (9 kJ/mol) are reached already for 100 solvating water molecules.

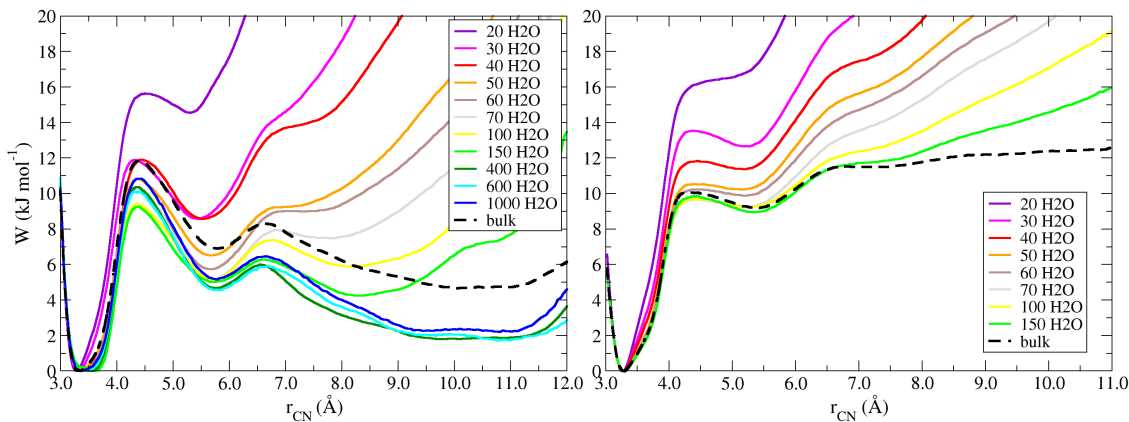


Figure 4.8. Free energy profiles for the Ac-Lys-Glu-NHMe dipeptide salt bridge opening in water clusters of different sizes obtained by umbrella sampling (left) and comparison to those for the $\text{NH}_4^+ \cdots \text{HCOO}^-$ pair (right). The free energy position of the contact pair minimum was set to 0.

The dependence of the dipeptide salt bridge free energy profile on cluster size (Fig. 4.8) is more complex than that for a single ion pair. For example the dependence

of the barrier height for the contact ion pair dissociation on the number of water molecules is not monotonous, but it decreases with increasing cluster size up to 150 water molecules, but then it starts increasing again. The free energy difference between the contact and the solvent shared minima decreases with increasing cluster size up to 600 water molecules, then increases again, still not being fully converged to the bulk value. From about 70 water molecules onward, a solvent separated ion pair appears. The corresponding minimum becomes deeper and shifts toward larger distances with increasing cluster size. The larger depth of the solvent shared ion pair minimum in comparison with $\text{NH}_4^+ \cdots \text{HCOO}^-$ in medium size clusters is probably due to the tendency of the CH_2 groups of the aliphatic parts to be exposed to the surface of the droplet. The significant solvent shared minimum is likely caused by the effect of configurational entropy of the side chains, because in this arrangement more conformations are accessible than either for the contact pair or the completely stretched chains.

To summarize, we explored the interplay between the neutral and zwitterionic states of a dipeptide salt bridge in small water clusters by BOMD simulations. Already a single water molecule can stabilize the charged side chain termini. We showed how the protonation state depends on the number of hydrogen bonds between the side chain termini, the water molecules, and the peptidic backbone. For larger clusters we described the salt bridge weakening employing free energy profiles from classical MD.

In this chapter, we combined BOMD simulations with enhanced sampling methods (and used classical MD for estimating the statistical uncertainties) to quantify the ion-ion and ion-peptide bond interactions in bulk water. Water molecules play more than just the role of spectators, this was demonstrated by, e.g., charge transfer from ions to solvent, binding arrangement of cations at the peptide bond, or proton transfer between the dipeptide side chains termini that can happen through a water bridge.

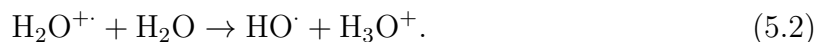
Chapter 5

DNA damage by ionizing radiation

The influence of exposure of cells to high energy radiation occurring during radiotherapy of cancer or coming from cosmic rays has witnessed much attention during the past decades. One of the major consequences of such impact is DNA ionization, i.e., an electron withdrawal [96]. Ionization and consequences thereof should be discriminated from electronic excitations caused by the UVB light leading to cross-links of two adjacent pyrimidine bases [97,98]. Not only DNA but all molecules (RH) within the cell can be ionized which leads to formation of radical cations(RH⁺):



The ejected electron can react fast with another molecule or become solvated first. The radical cation contains a “hole” which can be transferred, e.g., along the DNA strand or to another molecule. The radical cation can also lose a proton and become a neutral radical, as illustrated for the case of the initial radical cation produced by ionization of water (H₂O⁺) [99]:



The cellular DNA is damaged (Fig. 5.1) primarily via indirect mechanism by radicals produced by radiolysis of the solution, by HO· in particular, simply because water is much more abundant than DNA. HO· abstracts hydrogen from the deoxyribose sugar or adds to the double bonds of DNA. Attack at the sugar residue leads to fragmentation, base loss, and strand breaks [96] located on a single strand or even on both strands (double strand break). The latter type of damage is enabled by the

action of ionizing radiation which generates clusters of $\text{HO}\cdot$. This is an important distinction from spontaneous damage by reactive oxygen species which are unavoidable by-products of aerobic metabolism.

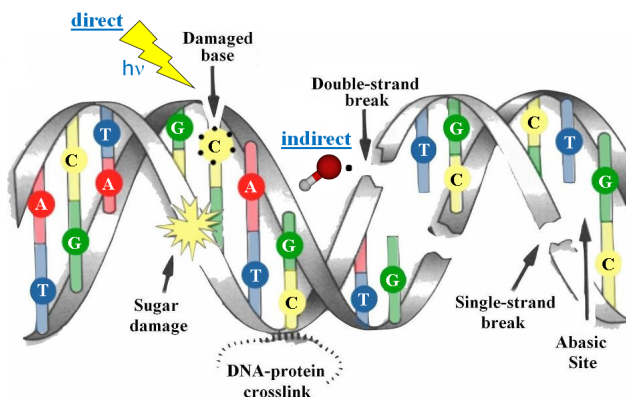


Figure 5.1. Mechanisms of radiation damage of DNA and illustration of various types of damage. Adapted from Christi A. Schroeder [100].

Direct ionization of DNA by an incoming photon creates a “hole” (a radical cation), mainly on the nucleobase, particularly on guanine which is the base most susceptible to ionization. The created “hole” (on whichever base) can migrate along the double-helix until it is trapped in an irreversible chemical reaction, typically leading to 8-oxo-guanine. To characterize and understand the radiation damage of DNA it is necessary to know the ionization energetics of each of its constituents in the native aqueous environment.

This chapter starts with description of creation and subsequent transformation of the cationic hole in pure water (Eq. 5.2). This requires combining BOMD simulations employing the CP2K software [33] for sampling the time evolution of the systems and higher level *ab initio* calculations for estimates of the corresponding spectral signatures. Then we proceed with the direct DNA damage and provide ionization energies of its constituents. Despite the complex nature of ionization and successive reactions the vertical ionization in solution can be captured employing selected, often minimized, geometries of the solute and continuum solvent. In other words, during a vertical processes nuclei do not have enough time to relax, which makes the description simpler allowing us to view water as a dielectric screening agent. In the last section we discuss the effect of moving the nucleobases from aqueous solution into a piece of aqueous DNA. All calculations regarding the direct DNA damage were performed using the Gaussian program package [101].

5.1 Cationic hole in water

This section deals with the formation of the cationic hole and its subsequent transformation in neat water as described by equations 5.1 and 5.2. This process has been little studied so far and most of the previous results were based on cluster calculations. To this end, we performed BOMD simulations of a bulk system modeled by 64 or 128 water molecules in a cubic box with periodic boundary conditions [102] (attached as the 7th publication). The initial conditions for the direct runs were taken from an equilibrated neutral water system. Subsequently, the system charge was switched to +1 which corresponds to vertical ionization of the least bound electron. The singly occupied orbital of the resulting open-shell system was treated employing the self-interaction correction.

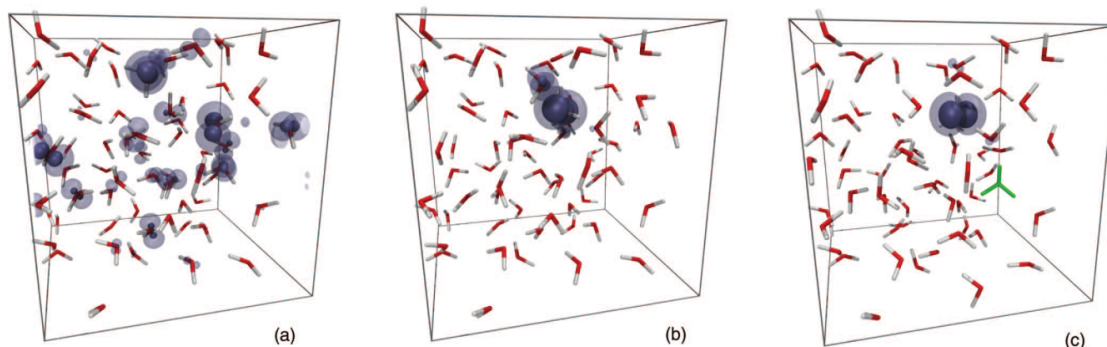


Figure 5.2. Snapshots from a typical trajectory of an ionized aqueous system with isosurfaces (at values of 0.01 and 0.001 au^{-3}) of the spin density. At $t = 0$ the hole is partially delocalized (a), but after 40 fs it localizes on a single water molecule forming H_2O^+ (b). Panel c) shows separated $\text{HO}\cdot$ and H_3O^+ (green) after 400 fs. Adapted from our publication [102].

The time evolution of the investigated system is illustrated on snapshots from a typical trajectory in Fig. 5.2. The spin density of the cationic hole is delocalized at time $t = 0$, but it localizes fast on a single molecule, forming H_2O^+ which then practically immediately provides a proton to a neighboring water molecule leading to formation of H_3O^+ and $\text{HO}\cdot$. This resulting contact pair later becomes separated by proton hopping from H_3O^+ to adjacent water molecules.

To quantify the process of the hole localization, we plotted the largest Mulliken spin population found on any water oxygen as a function of time for all trajectories (Fig. 5.3, left). The largest value of the spin population of 0.1–0.3 points to the hole delocalization over several water molecules, but after 31 fs (with a mean deviation of 21 fs) 95 % of the spin localizes on a single water molecule. Note that the extend of

the initial spin delocalization is dependent on the electronic structure method, which needs benchmarking for small cationic water clusters. The estimate of the spin density by the self-interaction-corrected BLYP method used in the BOMD simulations compares well with the benchmark EOM-IP-CCSD approach.

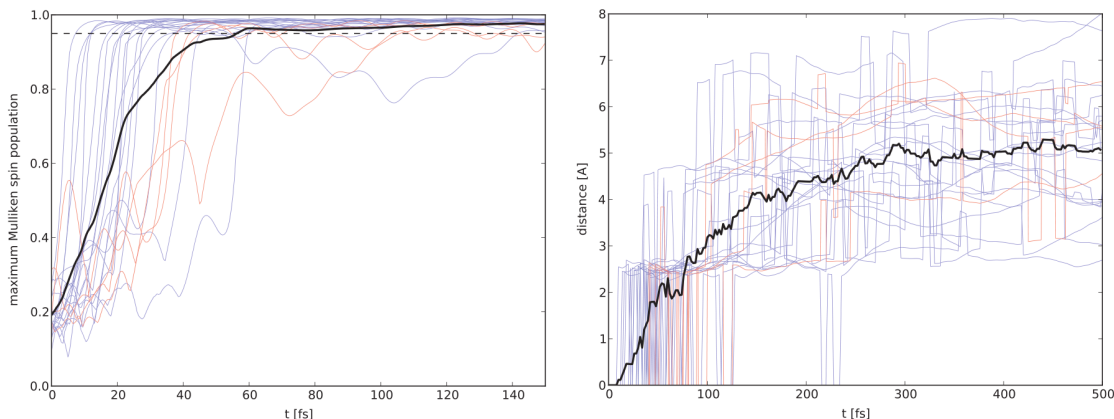


Figure 5.3. Maximum Mulliken spin population on a single oxygen atom (left) and the distance between the center of spin and the center of charge (right) as a function of time. DFT trajectories are depicted in blue, while trajectories collected employing DFT with empirical dispersion correction are red. The black line is the average over all trajectories.

The subsequent proton transfer reaction is characterized in the right panel of Fig. 5.3 which plots the separation of the center of spin from the center of charge against time. After the localization and before the proton transfer both charge and spin are situated at the same water molecule. After the first proton hop, which occurs on average at 33 fs (with a mean deviation of 14 fs), which practically coincides with the 95% localization time, the charge and spin become separated by ~ 2.6 Å corresponding to the length of a short hydrogen bond. A backward proton hop is observed for many trajectories and the final stabilization of the products occurs about 44 fs after the first proton transfer. Due to the omission of nuclear quantum effects, the proton transfer time and the number of re-crossings are likely to be overestimated, representing thus the upper bounds for these quantities.

To follow the above observations using experimentally measurable quantities, the spectrum of electronic excitations of a reactive subsystem was evaluated applying the EOM-IP-CCSD method with the rest of the system treated by point charges. As the reactive subsystem we have chosen a trimer composed from H_2O^+ and water molecules on which the proton may be transferred, being aware of the fact that such QM/MM decomposition is valid only after the partial spin localization. From the average of the time evolution of the electronic absorption spectra of each of

the trajectories, the localized $\text{H}_2\text{O}^{+\cdot}$ exhibits a weak feature between 2 and 2.5 eV which evolves to ~ 4 eV as $\text{H}_2\text{O}^{+\cdot}$ transforms to HO^\cdot . Unfortunately, the experimental signature of the localized hole was below the detection limit, probably due to the weak absorption by the short-lived transient species in comparison with solvated electrons which are produced during the experiment. Nevertheless, the presented results brought new insights into the very first stages following water ionization.

5.2 Direct ionization of DNA components

For investigation of the direct DNA damage we adopt a synthetic approach, i.e., starting from individual building blocks (a base, sugar, and phosphate) over a nucleoside and nucleotide, and finally to a piece of DNA (which is the topic of the next section). We also mention results from our previous publications [103, 104] in order to provide a complete picture of ionization characteristics of the DNA components. First we illustrate in Fig. 5.4, how the ionization energy and sometimes even stability of a given species depend on solvation and we also discuss limits of validity of the PCM approach (subsection 2.5.2).

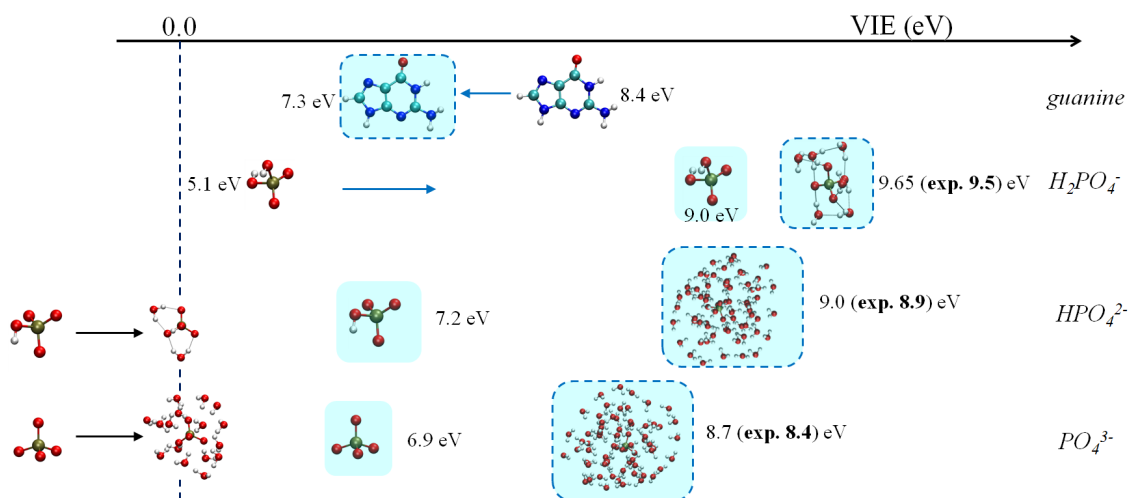


Figure 5.4. Stability, solvation, and vertical ionization energies of neutral and differently charged nucleic acid building blocks. Black arrows indicate solvent stabilization of species that do not exist per se, blue arrows label the process of solvation, light blue background stands for water modeled by PCM, and blue dashed margins mark the region beyond which the linear response regime can be safely assumed.

Solvation decreases the vertical ionization energy (VIE) of a neutral molecule, as indicated by a blue arrow for the example of guanine, because the resulting cation

is stabilized more strongly in solution than the original neutral molecule. Anions exhibit the opposite trend, because the species before ionization is more charged (in absolute value) and, therefore, better solvated. Multivalent phosphates (PO_4^{3-} and HPO_4^{2-}) do not exist as isolated species due to the Coulomb repulsion between the extra electrons which leads to a spontaneous electron loss. About two or three water molecules are needed for the HPO_4^{2-} ion and about 16 for the PO_4^{3-} ion to exist, such stabilization by microhydration is illustrated by black arrows in Fig. 5.4.

The multiply charged anions polarize their surroundings beyond the linear regime, which can be demonstrated by charge transfer to solvent in larger water clusters of 0.7 to 1.0 e as predicted by the Bader scheme. In such cases solvation using pure PCM is not theoretically justified and leads to considerable underestimating of the VIE. As a remedy, we gradually included explicit water molecules within the hybrid model to create a “buffer zone” beyond which water can be treated as a polarizable continuum. It turned out that about two solvation shells are required. For monovalent phosphate we expect better performance of the NEPCM for the VIE prediction due to the lower charge density. Actually, this approach provides an underestimate of only 0.5 eV in comparison with experiment and smaller dependence of the VIE on the number of explicit waters included in the hybrid model. Finally, for neutral molecules the effect of solvation is captured already by the pure PCM since the effect of specific short-range interactions with individual water molecules is less important than the long-range polarization of the continuum.

After testing applicability of the solvation models, we present in Fig. 5.5 ionization energies corresponding to ejection of the least bound electron for five nucleic acid bases in the aqueous environment and in the gas phase. The calculated VIEs of aqueous bases are distributed over less than 1 eV ranging from 7.3 eV for guanine to 8.1 eV for uracil. We also found it useful to estimate the energy change connected with the solvent and the solute nuclear relaxations, the sum of which is the difference between the vertical and adiabatic ionization energies in solution. The former contribution is slightly higher than 1 eV and dominates over the solute relaxation being below 0.4 eV. Upon moving to the gas phase, the VIE of a base increases by ~ 1 eV and the range of the values for the individual bases is slightly wider. The energy change accompanying the solute relaxation in the gas phase is comparable to that in water.

Once we determine the lowest ionization energy of the nucleobase, we continue exploration in two directions: ionization of more tightly bound electrons (subsection 2.5.1) and the influence of adding the sugar and phosphate moieties. Our manuscript [105] (attached as the 8th publication) presents a combined experimental

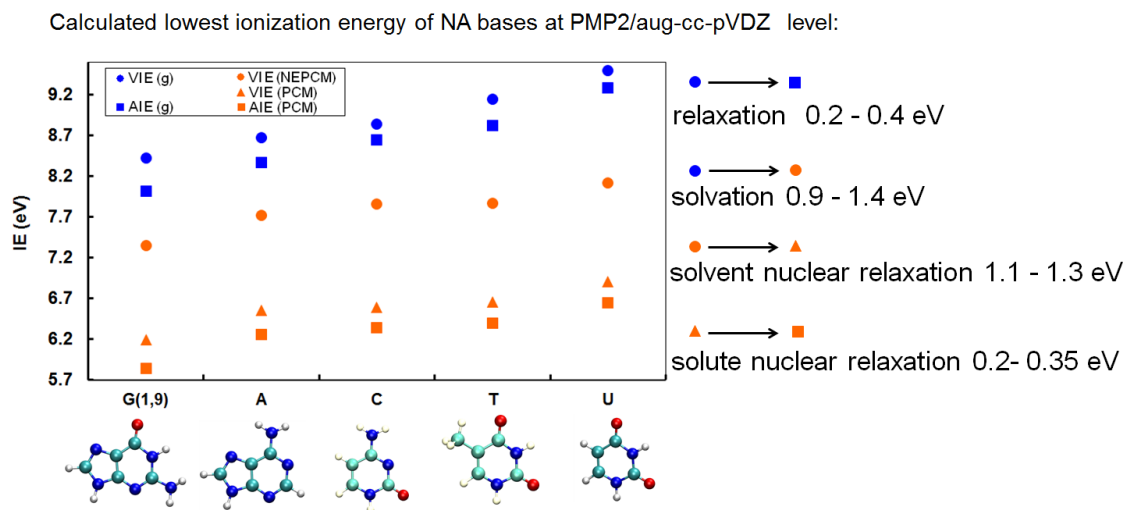


Figure 5.5. The lowest vertical (circles) and adiabatic (squares) ionization energies of nucleic acid bases in the gas phase (blue) and in the aqueous environment modeled by PCM (orange).

and theoretical study of photoionization of nucleosides and nucleotides in aqueous environment. Not all spectra are experimentally accessible because of low solubility or high cost of several of the investigated species, so theoretical predictions are helpful. Results are shown for adenine (Fig. 5.6) for which measurements for monovalent and divalent nucleotides are available.

The left panel depicts photoelectron spectra of aqueous adenosine, adenosine-monophosphate, and their constituents (adenine, ribose, and phosphate) with sticks indicating individual ionizations calculated within the NEPCM approach. The spectrum of the base consists of two bands, the first one being centered around the lowest ionization energy, while more ionization transitions contribute to the band in the higher binding energy region. The onsets of the spectra of ribose and phosphate are shifted by more than 1 eV towards higher binding energies in comparison with adenine. Adding sugar to the aqueous base upon forming nucleoside does not change the lowest VIE, but increases the intensity in the higher binding energy region. Both statements hold also for adding monovalent phosphate to the nucleoside.

Deprotonation of a monovalent nucleotide leading to a divalent species again does not affect the lowest VIE, but more transitions appear in the slightly higher binding energy region which changes the overall shape of the spectrum. However, as we have shown above, solvation of the divalent phosphate moiety by a pure continuum causes artificial lowering of its VIE, therefore, we employed a hybrid model with 50 water molecules around the phosphate group of the divalent nucleotide. This, depending

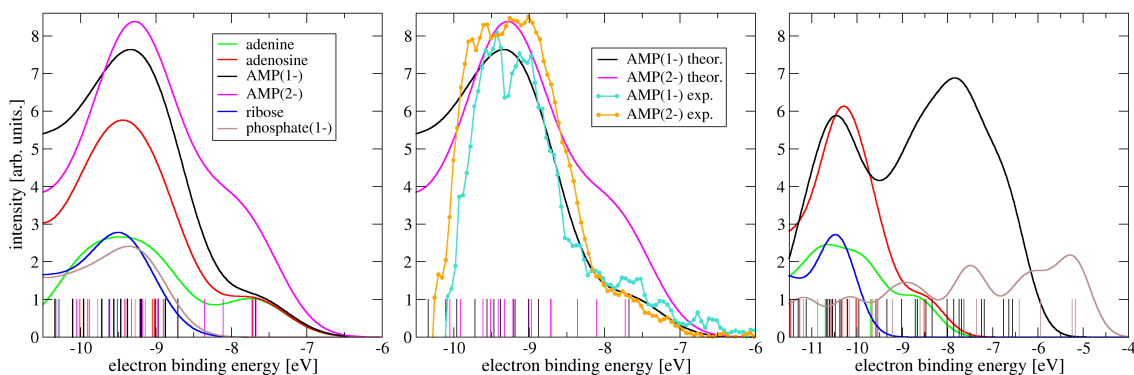


Figure 5.6. Simulated photoelectron spectra of adenine and its derivatives in aqueous environment (left) and in the gas phase (right) with sticks indicating individual transitions. Middle part shows comparison of theoretical and experimental nucleotide spectra.

on the configuration, increases the separation between the two lowest VIEs to 0.4–0.55 eV in comparison with a near degenerate situation without including explicit hydration. So we deduce that the intensity in the lower binding energy region should be smaller than plotted in Fig. 5.6. Assignment of VIEs of even more tightly bound electrons within the hybrid model is complicated by ionization originating from water molecules at the surface of the explicit water region, thus we can not make a more quantitative statement about this spectrum.

Based on all presented spectra we conclude that the lowest VIE originates from the base, which is also supported by the shape of the HOMO orbital. Adding ribose, mono- and even divalent phosphate does not influence this conclusion. The photoelectron spectra of more complex compounds in water can be roughly decomposed into contributions of the building blocks. Note, that in the higher binding energy region there are also transitions originating from a mixture of states from all constituents.

Theoretical predictions are compared with experimental results in the middle panel of Fig. 5.6. For the monovalent nucleotide, there is a good agreement both for the onset of the spectrum and the second broad and more intense band. The experimental spectrum of the divalent nucleotide is very similar to that of the monovalent one. The theoretical overestimation of the intensity of the first band can be attributed to the problematic description of solvation of the divalent moiety discussed above.

Upon dehydration (compare the left and the right panels of Fig. 5.6) significant changes happen. The VIEs of neutral molecules increase and those of anions decrease. Despite the destabilization of the nucleotide anion by presence of the phosphate group, according to the shape of the HOMO orbital, the lowest ionization still

originates from the base. The spectra of more complex molecules in the gas phase can no longer be decomposed into contributions of the constituents. This underlines the ability of the solvent to screen the interactions between the moieties leading to negligible influence of substitution and conformational isomerism [103] on the lowest VIE, and rough additivity of the spectra in water. Such observation is interesting from the modeling point of view, because it is usually expected that hydration complicates the description, while here the opposite is true.

Since ions in solution are always accompanied by their counterions (Na^+ in our case), we examined the effect of counterion binding on the ionization energy of differently charged phosphate ions [104] and nucleotides [105]. This effect turned out to be negligible in water. Photoelectron spectroscopy in aqueous solutions thus appears rather insensitive to ion pairing unlike, e.g., neutron scattering (Chapter 3).

Importantly, photoelectron spectra can be used to deduce one-electron redox potentials (i.e., AIEs referenced to the standard hydrogen electrode) which are together with reorganization energies (λ) necessary quantities for determination of the charge transfer process between the nucleobases in DNA. Such approach may seem too complicated and costly in comparison with standard electrochemical measurements, such as cyclic voltametry. However, based on our literature survey [105], the values of standard redox potentials have not been agreed upon, mainly because of difficulties caused by reactions following the initial electron removal. One of the problems, specifically water acting as a reactant in (de)protonation reactions, can be solved using acetonitrile [106], but the redox reactions still remain irreversible.

The reorganization energy can be estimated from photoionization in two ways. The first one has been illustrated in Fig. 5.5 and it is simply a sum of solute and solvent nuclear relaxation $\lambda = VIE - AIE$. The second way relies on the limit of linear response which relates the variance (σ^2) of the photoelectron peak fitted by a Gaussian to λ :

$$\sigma^2 = 2k_B T \lambda. \quad (5.3)$$

However, there are other contributions to the PE peak width than the reorganization energy. Therefore, we decided to combine experimental VIE and calculated λ within the polarizable continuum approach to get the most reliable estimate of the AIE and from it the redox potential after subtracting the absolute half cell potential of the standard hydrogen electrode relative to vacuum. Such approach provides a good agreement with redox potentials for guanine derivatives, which are the only cases with reliably eliminated follow-up reactions [107, 108]. Using this approach

we evaluated one-electron redox potentials for all bases, which do not suffer from irreversible reactions after electron removal. These are not only completing the table, but should help in further investigations of the charge transfer along the DNA strand.

Up to now, we dealt with the first step of radiation damage, i.e., the electron removal. The last part of this section is dedicated to the key product of radiation damage, namely 8-oxo-guanine (Fig. 5.7). On one hand, its presence can lead to mutations because of the base pair mismatch (i.e., Hoogsten pair with adenine instead of the standard one with cytosine) [109, 110]. On the other hand, it is more easily oxidized than guanine, hence, it can serve as a sink for the positive hole [111] and prevent other bases from oxidation. To our knowledge, the VIE of 8-oxo-guanine (8-oxoG) in the native aqueous environment has not been established yet, therefore, we present here our work in progress.

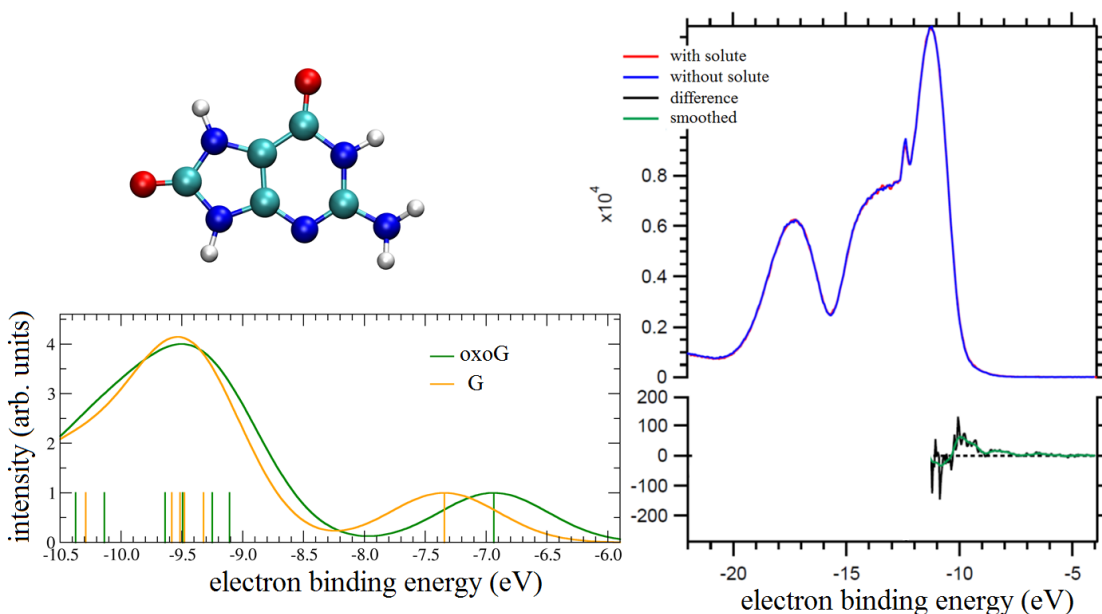


Figure 5.7. Structure of 8-oxoguanine (top, left), with its simulated photoelectron spectrum (green) compared to that of the parental base guanine (orange) in water. Right part shows the recorded photoelectron spectrum of buffered solution with and without 8-oxoguanine, the difference of the spectra, and its smoothing.

The simulated spectrum of 8-oxoG together with that of the parental base, guanine, is plotted in Fig. 5.7. Oxidation decreases the first VIE by about 0.4 eV. VIEs originating from more tightly bound electrons are shifted down as well, but less. Collected experimental spectra of a buffered solution with or without 8-oxoG and their difference are shown in the right part of Fig. 5.7. Unfortunately, due to the

low solubility, direct comparison of the less intense band in the lower binding energy region is not possible, but the predicted more intense band around 9 - 10 eV matches well the experiment.

To summarize this section, we critically examined performance of solvation models in context of photoionization and reported ionization energies and photoelectron spectra of aqueous nucleic acid components including an oxidation product. On concrete examples we demonstrated the ability of water to screen the interactions between the building blocks of more complex molecules. Finally, we suggested how to estimate the redox potentials of primary oxidation processes concerning DNA or its components.

5.3 Ionization of a piece of DNA

The next logical step after characterizing photoionization of individual nucleic acid components is to investigate a piece of DNA. In our work [112] (attached as the 9th publication), we chose the Dickerson dodecamer (DD) (Fig. 5.8) which is reasonably small, but already double helical and stable in water. Its structure was taken from reference [113], from which guanine (in ball and stick representation), or a GC base pair, or a GA stack were treated at the higher level of theory (MP2/aug-cc-pVDZ), while the remaining atoms of DD and neutralizing Na^+ counterions were described at the semi-empirical PM6 level, and water as a polarizable continuum. We intended to perform NEPCM calculations (analogous to the previous section), but NEPCM is not implemented yet with the employed procedure for treating the parts of the system at different levels of theory. Thus, we approximated the NEPCM ionization energy as the sum of the PCM ionization energy and the difference between NEPCM and PCM ionization energies of the whole DD treated at the semi-empirical level.

The predicted lowest VIE of guanine in the DNA environment of ~ 7 eV is almost the same as for the corresponding nucleotide (with the exact value depending on a particular conformer) and just a few tens of eV lower than that of corresponding nucleoside or base, as summarized in table 5.1. This potentially striking similarity points again to the screening ability of water which accounts for the major part of the influence of the environment.

Theoretical predictions are complemented by experimental measurements of a sheared DNA and an equimolar mixture of nucleotides (right part of Fig. 5.8). The spectra almost coincide with each other. Both have onset at VIE around ~ 7.5 eV,

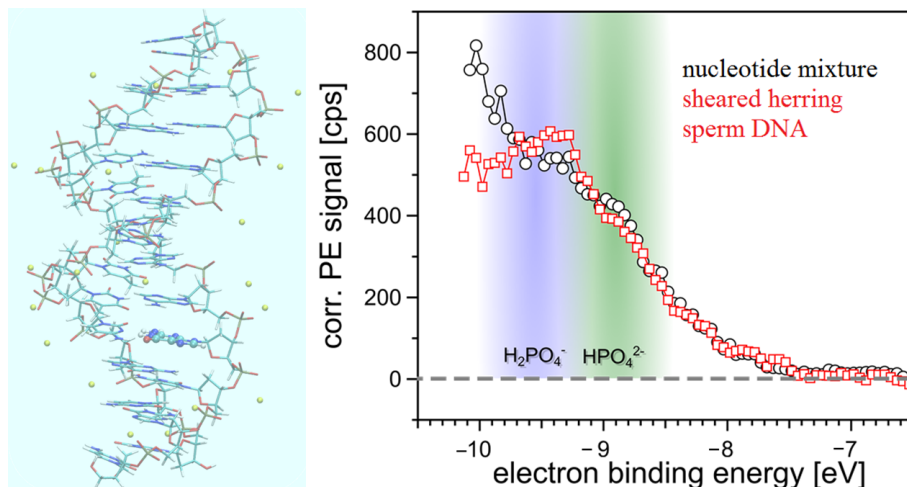


Figure 5.8. Structure of the Dickerson dodecamer (sticks) with Na^+ counterions (yellow spheres) in water modeled by a polarizable continuum (blue background), with ball and stick representation of guanine which is to be ionized (left). Experimental spectrum of a sheared DNA and an equimolar nucleotide mixture in buffered aqueous solution is also shown (right).

Table 5.1. Calculated vertical ionization energies of guanine in different environments in water (eV).

Guanine in DNA	7.1
Guanine in DNA (GC pair)	6.9
Guanine in DNA (GA stack)	7.0
Guanine in GMP^-	7.0 – 7.3
Guanine in guanosine	7.4
Guanine	7.3

which is slightly higher than values for guanine derivatives in Tab. 5.1, simply because of the larger molar fraction of bases with higher VIEs ([105] or Fig. 5.5). Note, that intensities at higher VIEs correspond to ionization originating from the sugar and phosphate moieties.

Next, we try to establish connection with previous quantum mechanics/molecular mechanics (QM/MM) calculations [114, 115] which despite a similar computational setup provided qualitatively different conclusions. Here, we put DD with counterions into bulk water and sample configurations of water molecules using classical MD with empirical FF with Na^+ ions not allowed to leave the contact ion pair region of the phosphate groups. From selected configurations we carved out DD with counterions

and water shells of increasing thickness as illustrated in Fig. 5.9 (left).

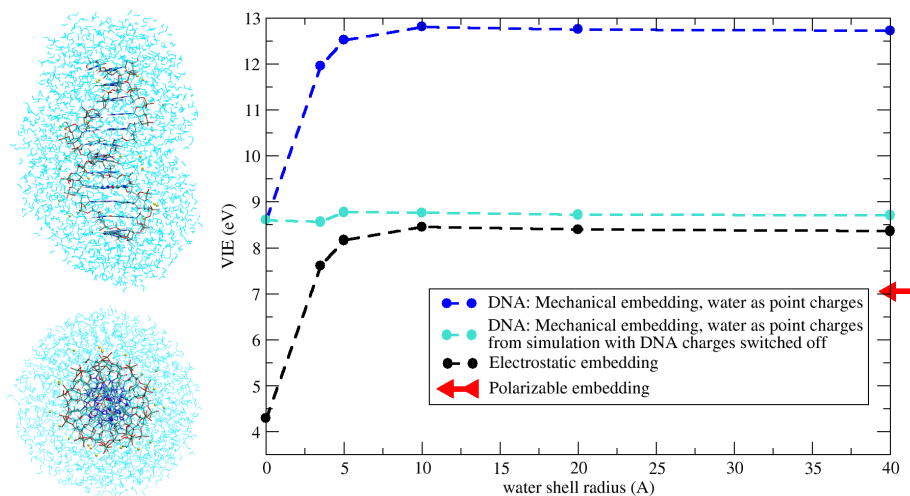


Figure 5.9. Left: front and bottom views of the Dickerson dodecamer and Na^+ counterions in a water shell. Right: VIE of guanine in the Dickerson dodecamer as a function the radius of the water shell included within electrostatic embedding. The effect of the DNA environment is treated either via mechanical embedding (blue) or electrostatic embedding (black). The former curve is compared with result obtained from sampling the solvation structure with DD and Na^+ charges switched off (light blue). The red arrow points to the value obtained from polarizable embedding designed in the present study.

Here, we treated only the base at an *ab initio* level, while the effect of the rest of DD with Na^+ counterions was modeled using electrostatic embedding or mechanical embedding, the former one including point charges from empirical FF. Water molecules were also represented by point charges. Within the full electrostatic embedding (black curve in Fig. 5.9), the VIE of guanine in dehydrated DD with Na^+ is by about 4 eV lower than in the gas phase (Fig. 5.5), which is mainly due to destabilization by nearby negatively charged phosphate groups. The VIE increases with the water shell radius and converges to ~ 8.5 eV at the $\sim 10\text{\AA}$ thickness. The resulting value of VIE is overestimated by about 1.5 eV which shows the importance of electronic polarization effects, in other words, the electronic relaxation is missing, so the value is “too vertical”. Treating the effect of DD with Na^+ just within mechanical embedding yields the dark blue curve in Fig. 5.9 which has the same qualitative shape as one discussed above, but is shifted by more than 4 eV towards higher energies. Our blue curve is surprisingly similar to that presented in reference [115]. It is, therefore, questionable, whether this large shift is caused by “complex molecular environment of DNA and solvent” as stated in Ref. [115] or potentially incomplete electrostatic embedding.

We were a little bit surprised, that VIE of a neutral base (with partial charges of the DNA environment switched off in the VIE calculation) has such a strong dependence on the degree of hydration. We speculated that it was due to the arrangement of water molecules which was sampled with charges switched on and, therefore, is influenced by the anionic character of the DNA backbone. To prove this, we performed additional MD sampling with the DD and Na⁺ partial charges being equal to 0, evaluated VIE using mechanical embedding and obtained the light blue curve in Fig. 5.9 which exhibits only a small dependence on the water shell radius as anticipated.

Present experimental and theoretical results on aqueous DNA show a surprisingly small effect of the DNA environment on the lowest VIE of guanine (the base most susceptible to ionization). This allows for using the VIEs determined for aqueous nucleotides in ionization processes involving DNA in its native environment.

Chapter 6

Conclusions

The core of the present thesis consists of nine papers dedicated to two phenomena: ion pairing and photoionization in aqueous solutions. In order to investigate them at a molecular level, we employed various methods of computational chemistry ranging from classical molecular dynamics simulations with empirical force fields with or without inclusion of polarization, over density functional theory (DFT) based Born-Oppenheimer molecular dynamics (BOMD), to *ab initio* calculations. To explore the configuration space of our model systems, we employed direct simulations, enhanced sampling techniques, or adopted a completely different approach, i.e., represented solvent as a structureless polarizable medium.

Before going through specific examples of systems interesting from chemical or biological points of view, we summarize the principal methodological contributions:

- Computationally cheap treatment of polarizability in an effective way by ionic charge rescaling provides qualitative improvement in the description of concentrated electrolyte solutions containing ions with high charged density over standard non-polarizable simulations. Affinity of soft ions to the aqueous solution/oil interface can be captured as well.
- DFT based BOMD can be combined with enhanced sampling methods, namely potential of mean force calculations or umbrella sampling, to obtain free energy profiles for ion-ion or ion-peptide bond dissociation. Auxilliary classical molecular dynamics simulations are helpful in estimating statistical uncertainties of such a procedure.
- The non-equilibrium polarizable continuum model of solvation performs well in context of photoionization, because it captures the long-range effects and distinguishes between the fast and the slow components of solvent response.

Incorporating moieties to be ionized into macromolecules in a polarizable way is also essential.

Turning now to the investigated systems, we first presented a combined classical molecular dynamics and neutron scattering study of concentrated lithium salt solutions. Employing ionic charge scaling within the electronic continuum correction (ECC) to account for polarization together with adjusting the ionic radii we obtained transferable force field parameters for Li^+ and Cl^- which reproduce well the structure of the solution deduced from the experiment. With such parameters we further analyzed hydration structures of these simple ions. Next, we applied the ECC for exploring behavior of the halide ions at the solution/air and solution/oil interface. This approach is theoretically well justified particularly in the latter case without a discrete jump in the electronic part of the dielectric constant and gives quantitatively correct results. In the former case with an electronic dielectric discontinuity the ECC approach overshoots the propensity of ions towards the interface, thus the predictions are only qualitative.

Next, we switched to the less parameter dependent BOMD simulations and enhanced sampling methods. For our first example, the geometrically simple, but electronically non-trivial lithium fluoride ion pair, we established the computational protocol for calculating the free energy profile as a potential of mean force along the ion-ion distance. Then, we utilized the information about electronic structure and exact interionic separations to evaluate the ionic charges along the dissociation path. Methodology presented here opens the way for BOMD simulations of more complex ion pairs. Next, we investigated interaction of the peptide bond with Na^+ and Ca^{2+} , because predictions from experiments and previous classical MD simulations were not in agreement with each other. We estimated the strength of cationic binding employing umbrella sampling and found for the two cations different geometries of contact pairs as a result of the competition between the waters and cation surrounding the carbonyl oxygen. Namely, Ca^{2+} almost always replaces all water molecules hydrogen-bonded to the carbonyl oxygen, while Na^+ only one. This leads for Na^+ to a tilted arrangement and to a negligible shift in the IR spectrum of the amide I band, unlike for Ca^{2+} . Our findings shed new light on rationalization of one of the key ion-specific Hofmeister effects and showed the importance of including the electronic structure information in MD simulations. Consequently, we investigated stability of a dipeptide salt bridge under different degrees of solvation which served as a model system for salt bridges in partially (de)hydrated protein pockets. We investigated the interplay between a neutral state, a strong salt bridge, and a weak salt bridge.

The titratable side chain residues of the bare dipeptide prefer to be neutral, but already a single water molecule causes proton transfer and stabilizes the zwitterionic state, if additional hydrogen bonding from the backbone is provided. Upon including more water molecules up to the bulk limit we quantified the salt bridge weakening, indicating that the salt bridge is most stable under moderately hydrated conditions.

Finally, we studied indirect and direct radiation damage to DNA in its native aqueous environment. We showed how the initially delocalized cationic hole in water localizes on a single molecule and then transfers proton to the neighboring water molecule upon formation of the HO \cdot which is the major cause of indirect (oxidative) destruction of DNA. Our project concerning the direct DNA damage started with theoretical and experimental photoelectron spectroscopy of aqueous nucleic acid building blocks, where we reported values of ionization energies, which despite their importance, were not known before. By comparison between gaseous and aqueous spectra we demonstrated ability of water to screen interactions between parts of more complex molecules. This causes negligible shift of the lowest ionization energy originating from the base upon addition of sugar or phosphate and rough additivity of the spectra. Finally, we observed only a small effect of the DNA environment on the lowest ionization energy of the base, which again shows that water accounts for the majority of environmental effects. This has significant implications for modeling of DNA where established values of ionization energies for individual nucleotides can be directly used.

To summarize, in this thesis we demonstrate how to use different simulation techniques to address issues of ion pairing and photoionization in water. Presented results shed new light on molecular interpretation of ion pairing, ion specific Hofmeister effects, and radiation damage to DNA.

List of Abbreviations

AIE	adiabatic ionization energy
AIMD	<i>ab initio</i> molecular dynamics
BOMD	Born-Oppenheimer molecular dynamics
CIP	contact ion pair
CP2K	Car-Parrinello molecular dynamics 2000 software for <i>ab initio</i> molecular dynamics
DD	Dickerson dodecamer
DFT	density functional theory
DNA	deoxyribonucleic acid
ECC	electronic continuum correction
Eq.	equation
FES	free energy surface
FF	force field
Fig.	figure
Glu	glutamic amino acid
HOMO	highest occupied molecular orbital
Lys	lysine amino acid
IE	ionization energy
IR	infrared
MD	molecular dynamics
MM	molecular mechanics
MP2	Møller-Plesset perturbation theory of the second order
NA	nucleic acid
NDIS	neutron diffraction with isotopic substitution
NEPCM	non-equilibrium polarizable continuum solvent model
NMA	N-methylacetamide
NPA	natural population analysis

PBC	periodic boundary conditions
PCM	polarizable continuum solvent model
PE	photoelectron
PES	potential energy surface
PMF	potential of mean force
QM	quantum mechanics
QM/MM	combination of QM and MM methods
RDF	radial distribution function
SIP	solvent shared ion pair
SOMO	singly occupied molecular orbital
TDDFT	time-dependent density functional theory
TS	transition state
VIE	vertical ionization energy
VMD	visualization molecular dynamics software

Bibliography

- [1] Y. Marcus and G. Hefter, “Ion pairing”, *Chemical Reviews* **2006**, *106*, 4585–4621.
- [2] N. Bjerrum, “Untersuchen uber ionenassoziation I.”, *K. Dan. Vidensk. Selsk.* **1926**, *7*, 1–48.
- [3] M. Eigen and K. Tamm, “Schallabsorption in Elektrolytlosungen als Folge Chemischer relaxation. 1. Relaxationstheorie der mehstufigen dissoziation”, *Zeitschrift für Elektrochemie* **1962**, *66*, 93–107.
- [4] K. S. Pitzer and G. Mayorga, “Thermodynamics of Electrolytes. 2. Activity and osmotic coefficients for strong electrolytes with one or both ions univalent”, *Journal of Physical Chemistry* **1973**, *77*, 2300–2308.
- [5] B. S. Krungalz, R. Pogorelsky, Y. A. Iosilevskii, A. Weiser, and K. S. Pitzer, “Ion-Interaction Approach for Volumetric Calculations for Solutions of Single Electrolytes at 25 Degrees C”, *Journal of Solution Chemistry* **1994**, *48*, 849–875.
- [6] I. Harsanyi, L. Temleitner, B. Beuneu, and L. Pusztai, “Neutron and X-ray diffraction measurements on highly concentrated aqueous LiCl solutions”, *Journal of Molecular Liquids* **2012**, *165*, 94–100.
- [7] S. Ansell, A. C. Barnes, P. E. Mason, G. W. Neilson, and S. Ramos, “X-ray and neutron scattering studies of the hydration structure of alkali ions in concentrated aqueous solutions”, *Biophysical Chemistry* **2006**, *124*, 171–179.
- [8] P. E. Mason, E. Wernersson, and P. Jungwirth, “Accurate Description of Aqueous Carbonate Ions: An Effective Polarization Model Verified by Neutron Scattering”, *Journal of Physical Chemistry B* **2012**, *116*, 8145–8153.
- [9] A. K. Soper and K. Weckstrom, “Ion solvation and water structure in potassium halide aqueous solutions”, *Biophysical Chemistry* **2006**, *124*, 180–191.
- [10] J. L. Fulton, S. M. Heald, Y. S. Badyal, and J. M. Simonson, “Understanding the effects of concentration on the solvation structure of Ca^{2+} in aqueous solution. I: The perspective on local structure from EXAFS and XANES”, *Journal of Physical Chemistry A* **2003**, *107*, 4688–4696.
- [11] V. T. Pham and J. L. Fulton, “Ion-pairing in aqueous CaCl_2 and RbBr solutions: Simultaneous structural refinement of XAFS and XRD data”, *Journal of Chemical Physics* **2013**, *138*, 044201.

-
- [12] W. Wachter, S. Fernandez, R. Buchner, and G. Hefter, “Ion association and hydration in aqueous solutions of LiCl and Li₂SO₄ by dielectric spectroscopy”, *Journal of Physical Chemistry B* **2007**, *111*, 9010–9017.
- [13] C. D. Waldburger, J. F. Schildbach, and R. T. Sauer, “Are buried salt bridges important for protein stability and conformational specificity”, *Nature Structural Biology* **1995**, *2*, 122–128.
- [14] W. C. Wimley, K. Gawrisch, T. P. Creamer, and S. H. White, “Direct measurement of salt-bridge solvation energies using a peptide model system: Implications for protein stability”, *Proceedings of the National Academy of Sciences* **1996**, *93*, 2985–2990.
- [15] A. Horovitz, L. Serrano, B. Avron, M. Bycroft, and A. R. Fersht, “Strength and cooperativity of contributions of surface salt bridges to protein stability”, *Journal of Molecular Biology* **1990**, *216*, 1031–1044.
- [16] Z. S. Hendsch and B. Tidor, “Do salt bridges stabilize proteins - A continuum electrostatic analysis”, *Protein Science* **1994**, *3*, 211–226.
- [17] H. Gong and K. F. Freed “Electrostatic Solvation Energy for Two Oppositely Charged Ions in a Solvated Protein System: Salt Bridges Can Stabilize Proteins”, *Biophysical Journal* **2010**, *98*, 470–477.
- [18] F. Hofmeister, “Zur Lehre von der Wirkung der Salze”, *Archiv für Experimentelle Pathologie und Pharmakologie* **1888**, *24*, 247–260.
- [19] B. Winter, R. Weber, W. Widdra, M. Dittmar, M. Faubel, and I. V. Hertel, “Full Valence Band Photoemission from Liquid Water Using EUV Synchrotron Radiation”, *Journal of Physical Chemistry A* **2004**, *108*, 2625–2632.
- [20] M. E. Tuckerman, “Statistical Mechanics: Theory and Molecular Simulation”, Oxford University Press Inc., New York **2010**.
- [21] P. P. Ewald, “Die Berechnung optischer und elektrostatischer Gitterpotentiale”, *Annalen der Physik* **1921**, *64*, 253–287.
- [22] U. Essmann, L. Perera, M. L. Berkowitz, T. Darden, H. Lee, and L. G. Pedersen. “A smooth particle mesh Ewald potential”, *Journal of Chemical Physics* **1995**, *103*, 8577–8592.
- [23] S. Kumar, J. M. Rosenberg, D. Bouzida, R. H. Swendsen, and P. A. Kollman, “The weighted histogram analysis method for free-energy calculations on biomolecules. I. The method”, *Journal of Computational Chemistry* **1992**, *13*, 1011–1021.
- [24] I. Nezbeda, J. Kolafa, and M. Kotrla, “Úvod do molekulárních simulací - Metody Monte Carlo a molekulární dynamiky”, Karolinum, Praha **2003**.
- [25] J. E. Enderby and G. W. Neilson, “The structure of electrolyte solutions”, *Reports on Progress in Physics* **1981**, *44*, 593–653.
- [26] M. Karplus, “Molecular dynamics simulations of biomolecules”, *Accounts of Chemical Research* **2002**, *35*, 321–323.
- [27] T. Simonson and C. L. Brooks, “Charge screening and the dielectric constant of proteins: Insights from molecular dynamics”, *Journal of American Chemical Society* **1996**, *118*, 8452–8458.

-
- [28] F. T. H. Leuwerink and W. J. Briels “Dielectric constant and structure of liquid 18-crown-6 calculated from molecular dynamics simulations”, *Journal of Physical Chemistry B* **1997**, *101*, 1024–1034.
- [29] H. Nymeyer and H. X. Zhou, “A method to determine dielectric constants in nonhomogeneous systems: Application to biological membranes”, *Biophysical Journal* **2008**, *94*, 1185–1193.
- [30] I. V. Leontyev and A. A. Stuchebrukhov, “Electronic continuum model for molecular dynamics simulations”, *Journal of Chemical Physics* **2009**, *130*, 085102.
- [31] I. V. Leontyev and A. A. Stuchebrukhov, “Electronic Continuum Model for Molecular Dynamics Simulations of Biological Molecules”, *Journal of Chemical Theory and Computation* **2010**, *6*, 1498–1508.
- [32] I. V. Leontyev and A. A. Stuchebrukhov, “Accounting for electronic polarization in non-polarizable force fields”, *Physical Chemistry Chemical Physics* **2011**, *13*, 2613–2626.
- [33] J. VandeVondele, M. Krack, F. Mohamed, M. Parrinello, T. Chassaing, and J. Hutter, “QUICKSTEP: Fast and accurate density functional calculations using a mixed Gaussian and plane waves approach”, *Computer Physics Communications* **2005**, *167*, 103–128.
- [34] S. Goedecker, M. Teter, and J. Hutter, “Separable dual-space Gaussian pseudopotentials”, *Physical Review B* **1996**, *54*, 1703–1710.
- [35] J. L. McHale, “Molecular spectroscopy”, Prentice Hall **1998**.
- [36] H. B. Schlegel, “Møller-Plesset Perturbation Theory with Spin Projection”, *Journal of Physical Chemistry* **1988**, *92*, 3075–3078.
- [37] M. Kamiya and S. Hirata “Higher-order equation-of-motion coupled-cluster methods for ionization processes”, *Journal of Chemical Physics* **2006**, *125*, 074111.
- [38] K. B. Bravaya, O. Kostko, M. Ahmed, and A. I. Krylov, “The effect of pi-stacking, H-bonding, and electrostatic interactions on the ionization energies of nucleic acid bases: adenine-adenine, thymine-thymine and adenine-thymine dimers”, *Physical Chemistry Chemical Physics* **2010**, *12*, 2261–2504.
- [39] W. von Niessen, J. Schirmer, and L. S. Cederbaum, “Computational methods for the onr-particle Green-function”, *Computer Physics Reports* **1984**, *1*, 57–125.
- [40] O. Dolgounitcheva, V. G. Zakrzewski, and J. V. Ortiz, “Vertical Ionization Energies of Adenine and 9-Methyl Adenine”, *Journal of Physical Chemistry A* **2009**, *113*, 14630–14635.
- [41] J. V. Ortiz, “Partial third-order quasiparticle theory: Comparisons for closed-shell ionization energies and an application to the Borazine photoelectron spectrum”, *Journal of Chemical Physics* **1996**, *104*, 7599–7605.
- [42] J. Schirmer, L. S. Cederbaum, and O. Walter, “New approach to the one-particle Greens-function for finite Fermi systems”, *Physical Review A* **1983**, *28*, 1237–1259.
- [43] P. Slavíček, B. Winter, M. Faubel, S. E. Bradforth, and P. Jungwirth, “Ionization energies of aqueous nucleic acids: Photoelectron spectroscopy of pyrimidine nucleosides and ab initio calculations”, *Journal of American Chemical Society* **2009**, *131*, 6460–6467.

-
- [44] D. Roca-Sanjuan, M. Rubio, M. Merchan, and L. Serrano-Andres, “Ab initio determination of the ionization potentials of DNA and RNA nucleobases”, *Journal of Chemical Physics* **2006**, *125*, 084302.
- [45] B. Winter and M. Faubel, “Photoemission from Liquid Aqueous Solutions”, *Chemical Reviews* **2006**, *106*, 1176–1211.
- [46] P. Hunt, M. Sprik, and R. Vuilleumier, “Thermal versus electronic broadening in the density of states of liquid water”, *Chemical Physics Letters* **2003**, *376*, 68–74.
- [47] S. Barth, M. Ončák, V. Ulrich, M. Mucke, T. Lischke, P. Slavíček, and U. Hergenbahn, “Valence Ionization of Water Clusters: From Isolated Molecules to Bulk”, *Journal of Physical Chemistry A* **2009**, *113*, 13519–13527.
- [48] M. Cossi and V. Barone, “Solvent effect on vertical electronic transitions by the polarizable continuum model”, *Journal of Chemical Physics* **2000**, *112*, 2427–2435.
- [49] M. Cossi and V. Barone, “Separation between Fast and Slow Polarizations in Continuum Solvation Models”, *Journal of Physical Chemistry A* **2000**, *104*, 10614–10622.
- [50] J. Tomasi, B. Mennucci, and R. Cammi, “Quantum Mechanical Continuum Solvation Models”, *Chemical Reviews* **2005**, *105*, 2999–3093.
- [51] R. Seidel, S. Thürmer, and B. Winter, “Photoelectron Spectroscopy Meets Aqueous Solution: Studies from a Vacuum Liquid Microjet”, *Journal of Physical Chemistry Letters* **2011**, *2*, 633–641.
- [52] P. W. Palmberg and T. N. Rhodin, “Auger Electron Spectroscopy of Fcc Metal Surfaces”, *Journal of Applied Physics* **1968**, *39*, 2425.
- [53] N. Ottosson, M. Faubel, S. E. Bradforth, P. Jungwirth, and B. Winter, “Photoelectron spectroscopy of liquid water and aqueous solution: Electron effective attenuation lengths and emission-angle anisotropy”, *Journal of Electron Spectroscopy and Related Phenomena* **2010**, *177*, 60–70.
- [54] B. Hess, C. Kutzner, D. van der Spoel, and E. Lindahl, “GROMACS 4: Algorithms for Highly Efficient, Load-Balanced, and Scalable Molecular Simulation”, *Journal of Chemical Theory and Computation* **2008**, *4*, 435–447.
- [55] M. S. Whittingham, “Lithium Batteries and Cathode Materials”, *Chemical Reviews* **2004**, *104*, 4271–4301.
- [56] S. Ansell, A. C. Barnes, P. E. Mason, G. W. Neilson, and S. Ramos, “X-ray and Neutron Scattering Studies of the Hydration Structure of Alkali Ions in Concentrated Aqueous Solutions”, *Biophysical Chemistry* **2006**, *124*, 171–179.
- [57] I. Harsanyi and L. Pusztai, “Hydration Structure in Concentrated Aqueous Lithium Chloride Solutions: A Reverse Monte Carlo Based Combination of Molecular Dynamics Simulations and Diffraction Data”, *Journal of Chemical Physics* **2012**, *137*, 204503.
- [58] S. Bouazizi and S. Nasr, “Local Order in Aqueous Lithium Chloride Solutions as Studied by X-ray Scattering and Molecular Dynamics Simulation”, *Journal of Molecular Structure* **2007**, *837*, 206–213.

-
- [59] I. Harsanyi and L. Pusztai, “On the Structure of Aqueous LiCl Solutions”, *Journal of Chemical Physics* **2005**, *122*, 124512.
- [60] A. V. Egorov, A. V. Komolkin, and V. I. Chizhik, “Influence of Temperature on the Microstructure of the Lithium-Ion Hydration Shell. A Molecular Dynamics Description”, *Journal of Molecular Liquids* **2000**, *89*, 47–55.
- [61] S. Ansell, P. E. Mason, G. W. Neilson, and S. Rempe, **2013**, *submitted*.
- [62] E. Pluhařová, P. E. Mason, P. Jungwirth, “Ion Pairing in Aqueous Lithium Salt Solutions with Monovalent and Divalent Counter-Anions”, *Journal of Physical Chemistry A* **2013**, *117*, 11766–11773 .
- [63] W. L. Jorgensen, “OPLS and OPLS-AA Parameters for Organic Molecules, Ions, and Nucleic Acids”, *Yale University* **1997**.
- [64] L. X. Dang, J. E. Rice, J. Caldwell, and P. A. Kollman “Ion Solvation in Polarizable Water - Molecular-Dynamics Simulations”, *Journal of the American Chemical Society* **1991**, *113*, 2481–2486.
- [65] I. Harsanyi, P. A. Bopp, A. Vrhovsek, and L. Pusztai, “On the hydration structure of LiCl aqueous solutions: A Reverse Monte Carlo based combination of diffraction data and Molecular Dynamics simulations”, *Journal of Molecular Liquids* **2011**, *158*, 61–67.
- [66] F. Bruni, S. Imberti, R. Mancinelli, and M. A. Ricci, “Aqueous solutions of divalent chlorides: Ions hydration shell and water structure”, *Journal of Chemical Physics* **2012**, *136*, 064520.
- [67] R. Mancinelli, A. Botti, F. Bruni, M. A. Ricci, and A. K. Soper, “Hydration of sodium, potassium, and chloride ions in solution and the concept of structure maker/breaker”, *Journal of Physical Chemistry B* **2007**, *111*, 13570–13577.
- [68] S. Tazi, J. J. Molina, B. Rotenberg, P. Turq, R. Vuilleumier, and M. Salanne, “A transferable ab-initio based force field for aqueous ions”, *Journal of Chemical Physics* **2012**, *136*, 114507.
- [69] D. H. Powell, G. W. Neilson, and J. E. Enderby, “The structure of Cl⁻ in aqueous solution: an experimental determination of $g_{ClH}(r)$ and $g_{ClO}(r)$ ”, *Journal of Physics: Condensed Matter* **1993**, *5*, 5723.
- [70] E. Pluhařová, H. E. Fischer, P. E. Mason, and P. Jungwirth, “Hydration of the Chloride Ion in Concentrated Aqueous Solutions using Neutron Scattering and Molecular Dynamics”, *Molecular Physics* **2014**, *112*, 1230–1240.
- [71] L. X. Dang, B. M. Pettitt, and P. J. Rossky, “On the correlation between like ion pairs in water”, *Journal of Chemical Physics* **1992**, *96*, 4046–4047.
- [72] L. Vrbka, M. Mucha, B. Minofar, P. Jungwirth, E. C. Brown, and D. J. Tobias, “Propensity of Soft Ions for the Air/Water Interface”, *Current Opinion in Colloid & Interface Science* **2004**, *9*, 67–73.
- [73] D. E. Otten, P. R. Shaffer, P. L. Geissler, and R. J. Saykally, “Elucidating the mechanism of selective ion adsorption to the liquid water surface”, *Proceedings of the National Academy of Sciences of the United States of America* **2012**, *109*, 701–705.

-
- [74] M. Vazdar, E. Pluhařová, P. E. Mason, R. Vácha, and P. Jungwirth, “Ions at Hydrophobic Aqueous Interfaces: Molecular Dynamics with Effective Polarization”, *Journal of Physical Chemistry Letters* **2012**, *3*, 2087–2091.
- [75] W. G. Scaife, “The relative permittivity of the n alkanes from n pentane to n decane as a function of pressure and temperature”, *Journal of Physics Part A General* **1972**, *5*, 897–903.
- [76] R. Aveyard and S. M. Saleem, “Interfacial tensions at alkane-aqueous electrolyte interfaces”, *Journal of the Chemical Society – Faraday Transactions I* **1976**, *72*, 1609–1617.
- [77] J. VandeVondele and J. Hutter, “Gaussian basis sets for accurate calculations on molecular systems in gas and condensed phases”, *Journal of Chemical Physics* **2007**, *127*, 114105.
- [78] A. D. Becke, “Density-functional exchange-energy approximation with correct asymptotic behavior”, *Physical Review A* **1988**, *38*, 3098–3100.
- [79] C. T. Lee, W. T. Yang, and R. G. Parr, “Development of the Colle-Salvetti correlation-energy formula into a functional of the electron density”, *Physical Review B* **1988**, *37*, 785–789.
- [80] S. Grimme, “Semiempirical GGA-type density functional constructed with a long-range dispersion correction”, *Journal of Computational Chemistry* **2006**, *27*, 1787–1799.
- [81] E. Pluhařová, O. Marsalek, B. Schmidt, and P. Jungwirth, “Ab Initio Molecular Dynamics Approach to a Quantitative Description of Ion Pairing in Water”, *Journal of Physical Chemistry Letters* **2013**, *4*, 4177–4181.
- [82] J. Timko, D. Bucher, S. Kuyucak, “Dissociation of NaCl in water from ab initio molecular dynamics simulations”, *Journal of Chemical Physics* **2010**, *132*, 114510.
- [83] J. Timko, A. De Castro, and S. Kuyucak, “Ab initio calculation of the potential of mean force for dissociation of aqueous Ca-Cl”, *Journal of Chemical Physics* **2011**, *134*, 204510.
- [84] I. S. Joung and T. E. Cheatham, “Determination of alkali and halide monovalent ion parameters for use in explicitly solvated biomolecular simulations”, *Journal of Physical Chemistry B* **2008**, *112*, 9020–9041.
- [85] R. F. Bader, “Atoms in Molecules - A quantum theory”, Oxford University Press: New York, **1990**.
- [86] A. E. Reed, R. B. Weinstock, and F. Weinhold, “Natural population analysis”, *The Journal of Chemical Physics* **1985**, *83*, 735–746.
- [87] L. M. Pegram, and M. T. Record, “Hofmeister salt effects on surface tension arise from partitioning of anions and cations between bulk water and the air-water interface”, *Journal of Physical Chemistry B* **2007**, *111*, 5411–5417.
- [88] J. Heyda, J. C. Vincent, D. J. Tobias, J. Dzubiella, and P. Jungwirth, “Ion Specificity at the Peptide Bond: Molecular Dynamics Simulations of N-Methylacetamide in Aqueous Salt Solutions”, *Journal of Physical Chemistry B* **2010**, *114*, 1213–1220.
- [89] E. A. Algaer, and N. F. A. van der Vegt, “Hofmeister Ion Interactions with Model Amide Compounds”, *Journal of Physical Chemistry B* **2011**, *115*, 13781–13787.

- [90] H. I. Okur, J. Kherb, and P. S. Cremer, “Cations Bind Only Weakly to Amides in Aqueous Solutions”, *Journal of the American Chemical Society* **2013**, *135*, 5062–5067.
- [91] E. Pluhařová, M. D. Baer, C. J. Mundy, B. Schmidt, and P. Jungwirth, “Aqueous Cation-Amide Binding: Free Energies and IR Spectral Signatures by Ab Initio Molecular Dynamics”, *Journal of Physical Chemistry Letters* **2014**, *5*, 2235–2240.
- [92] M. P. Gaigeot, R. Vuilleumier, M. Sprik, and D. Borgis, “Infrared spectroscopy of N-methylacetamide revisited by ab initio molecular dynamics simulations”, *Journal of Chemical Theory and Computation* **2005**, *1*, 772–789.
- [93] G. Mathias and M. D. Baer, “Generalized Normal Coordinates for the Vibrational Analysis of Molecular Dynamics Simulations”, *Journal of Chemical Theory and Computation* **2011**, *7*, 2028–2039.
- [94] J. VandeVondele, P. Troster, P. Tavan, and G. Mathias, “Vibrational Spectra of Phosphate Ions in Aqueous Solution Probed by First-Principles Molecular Dynamics”, *Journal of Physical Chemistry A* **2012**, *116*, 2466–2474.
- [95] E. Pluhařová, O. Marsalek, B. Schmidt, and P. Jungwirth, “Peptide salt bridge stability: From gas phase via microhydration to bulk water simulations”, *Journal of Chemical Physics* **2012**, *137*, 185101.
- [96] E. C. Friedberg, G. C. Walker, W. Siede, R. D. Wood, R. A. Schultz, and T. Ellenberger, “DNA Repair and Mutagenesis”, Second Edition, ASM Press, Washington, D. C. **2006**.
- [97] K. H. Kraemer, “Sunlight and skin cancer: Another link revealed”, *Proc. Natl. Acad. Sci. USA* **1997**, *94*, 11–14.
- [98] R. P. Sinha and D. P. Hader “UV-induced DNA damage and repair: a review”, *Photochemical and Photobiological Sciences* **2002**, *1*, 225–236.
- [99] B. C. Garrett, D. A. Dixon, D. M. Camaioni, D. M. Chipman, M. A. Johnson, C. D. Jonah, G. A. Kimmel, J. H. Miller, T. N. Rescigno, P. J. Rossky, S. S. Xantheas, S. D. Colson, A. H. Laufer, D. Ray, P. F. Barbara, D. M. Bartels, K. H. Becker, K. H. Bowen, Jr., S. E. Bradforth, I. Carmichael, J. V. Coe, L. R. Corrales, J. P. Cowin, M. Dupuis, K. B. Eisenthal, J. A. Franz, M. S. Gutowski, K. D. Jordan, B. D. Kay, J. A. LaVerne, S. V. Lyman, T. E. Madey, C. W. McCurdy, D. Meisel, S. Mukamel, A. R. Nilsson, T. M. Orlando, N. G. Petrik, S. M. Pimblott, J. R. Rustad, G. K. Schenter, S. J. Singer, A. Tokmakoff, L.-S. Wang, C. Wittig, and T. S. Zwier, “Role of Water in Electron-Initiated Processes and Radical Chemistry: Issues and Scientific Advances”, *Chemical Reviews* **2005**, *105*, 355–389.
- [100] C. A. Schroeder, “Quantifying Aspects of DNA damage”, Dissertation thesis, University of Southern California, Los Angeles **2012**.
- [101] M. J. Frisch, G. W. Trucks, H. B. Schlegel, G. E. Scuseria, M. A. Robb, J. R. Cheeseman, J. A. Montgomery, Jr., T. Vreven, K. N. Kudin, J. C. Burant, J. M. Millam, S. S. Iyengar, J. Tomasi, V. Barone, B. Mennucci, M. Cossi, G. Scalmani, N. Rega, G. A. Petersson, H. Nakatsuji, M. Hada, M. Ehara, K. Toyota, R. Fukuda, J. Hasegawa, M. Ishida, T. Nakajima, Y. Honda, O. Kitao, H. Nakai, M. Klene, X. Li, J. E. Knox, H. P. Hratchian, J. B. Cross, V. Bakken, C. Adamo, J. Jaramillo, R. Gomperts, R. E. Stratmann, O. Yazyev,

- A. J. Austin, R. Cammi, C. Pomelli, J. W. Ochterski, P. Y. Ayala, K. Morokuma, G. A. Voth, P. Salvador, J. J. Dannenberg, V. G. Zakrzewski, S. Dapprich, A. D. Daniels, M. C. Strain, O. Farkas, D. K. Malick, A. D. Rabuck, K. Raghavachari, J. B. Foresman, J. V. Ortiz, Q. Cui, A. G. Baboul, S. Clifford, J. Cioslowski, B. B. Stefanov, G. Liu, A. Liashenko, P. Piskorz, I. Komaromi, R. L. Martin, D. J. Fox, T. Keith, M. A. Al-Laham, C. Y. Peng, A. Nanayakkara, M. Challacombe, P. M. W. Gill, B. Johnson, W. Chen, M. W. Wong, C. Gonzalez, and J. A. Pople, "Gaussian 03, Revision E.01", Gaussian, Inc., Wallingford, CT, **2004**.
- [102] O. Marsalek, C. G. Elles, P. A. Pieniazek, E. Pluhařová, J. VandeVondele, S. E. Bradforth, and P. Jungwirth, "Chasing charge localization and chemical reactivity following photoionization in liquid water", *Journal of Chemical Physics* **2011**, *135*, 224510.
- [103] E. Pluhařová, S. E. Bradforth, P. Jungwirth, and P. Slavíček, "Ionization of purine tautomers in nucleobases, nucleosides, and nucleotides: from the gas phase to the aqueous environment", *Journal of Physical Chemistry B* **2011**, *115*, 1294-1305.
- [104] E. Pluhařová, M. Ončák, R. Seidel, C. Schroeder, W. Schroeder, B. Winter, S. E. Bradforth, P. Jungwirth and P. Slavíček, "Transforming Anion Instability into Stability: Contrasting Photoionization of Three Protonation Forms of the Phosphate Ion upon Moving into Water", *Journal of Physical Chemistry B* **2012**, *116*, 13254—13264.
- [105] C. A. Schroeder, E. Pluhařová, R. Seidel, W. P. Schroeder, B. Winter, M. Faubel, P. Slavíček, P. Jungwirth, and S. E. Bradforth, "Photoelectron spectroscopy of pyrimidine and purine nucleotides and their component parts in buffered aqueous solution", **2014**, *submitted*.
- [106] C. A. M. Seidel, A. Schulz, and M. H. M. Sauer, "Nucleobase-Specific Quenching of Fluorescent Dyes. 1. Nucleobase One-Electron Redox Potentials and Their Correlation with Static and Dynamic Quenching Efficiencies", *Journal of Physical Chemistry* **1996**, *100*, 5541–5553.
- [107] S. Steenken and S. V. Jovanovic, "How Easily Oxidizable Is DNA? One-Electron Reduction Potentials of Adenosine and Guanosine Radicals in Aqueous Solution", *Journal of American Chemical Society* **1997**, *119*, 617–618.
- [108] B. T. Psciuk, R. L. Lord, B. H. Munk, and H. B. Schlegel, "Theoretical Determination of One-Electron Oxidation Potentials for Nucleic Acid Bases", *Journal of Chemical Theory and Computation* **2012**, *8*, 5107–5123.
- [109] W. L. Neeley and J. M. Essigmann, "Mechanisms of formation, genotoxicity, and mutation of guanine oxidation products", *Chemical Research in Toxicology* **2006**, *19*, 491–505.
- [110] S. D. Bruner, D. P. G. Norman, and G. L. Verdine, "Structural basis for recognition and repair of the endogenous mutagen 8-oxoguanine in DNA", *Nature* **2000**, *403*, 859–866.
- [111] S. Steenken, S. V. Jovanovic, M. Bietti, and K. Bernhard, "The trap depth (in DNA) of 8-oxo-7,8-dihydro-2'-deoxyguanosine as derived from electron-transfer equilibria in aqueous solution", *Journal of the American Chemical Society* **2000**, *122*, 2373–2374.
- [112] E. Pluhařová, C. A. Schroeder, R. Seidel, S. E. Bradforth, B. Winter, M. Faubel, P. Slavíček, and P. Jungwirth, "Unexpectedly Small Effect of the DNA Environment on Vertical Ionization Energies of Aqueous Nucleobases", *Journal of Physical Chemistry Letters* **2013**, *4*, 3766—3769.

- [113] N. Tjandra, S. Tate, A. Ono, M. Kainosho, and A. Bax, “The NMR structure of a DNA dodecamer in an aqueous dilute liquid crystalline phase”, *Journal of the American Chemical Society* **2000**, *122*, 6190–6200.
- [114] D. Roca-Sanjuan, G. Olaso-Gonzalez, M. Rubio, P. B. Coto, M. Merchan, N. Ferre, V. Ludwig, and L. Serrano-Andres, “DNA Nucleobase Properties and Photoreactivity: Modeling Environmental Effects”, *Pure and Applied Chemistry* **2009**, *81*, 743–754.
- [115] E. Cauet, M. Valiev, and J. H. Weare, “Vertical Ionization Potentials of Nucleobases in a Fully Solvated DNA Environment”, *Journal of Physical Chemistry B* **2010**, *114*, 5886–5894.

List of Attached Publications

1. E. Pluhařová, P. E. Mason, P. Jungwirth, “Ion Pairing in Aqueous Lithium Salt Solutions with Monovalent and Divalent Counter-Anions”, *Journal of Physical Chemistry A* **2013**, *117*, 11766—11773.
2. E. Pluhařová, H. E. Fischer, P. E. Mason, and P. Jungwirth, “Hydration of the Chloride Ion in Concentrated Aqueous Solutions using Neutron Scattering and Molecular Dynamics”, *Molecular Physics* **2014**, *112*, 1230–1240.
3. M. Vazdar, E. Pluhařová, P. E. Mason, R. Vácha, and P. Jungwirth, “Ions at Hydrophobic Aqueous Interfaces: Molecular Dynamics with Effective Polarization”, *Journal of Physical Chemistry Letters* **2012**, *3*, 2087–2091.
4. E. Pluhařová, O. Marsalek, B. Schmidt, and P. Jungwirth, “Ab Initio Molecular Dynamics Approach to a Quantitative Description of Ion Pairing in Water”, *Journal of Physical Chemistry Letters* **2013**, *4*, 4177–4181.
5. E. Pluhařová, M. D. Baer, C. J. Mundy, B. Schmidt, and P. Jungwirth, “Aqueous Cation-Amide Binding: Free Energies and IR Spectral Signatures by Ab Initio Molecular Dynamics”, *Journal of Physical Chemistry Letters* **2014**, *5*, 2235–2240.
6. E. Pluhařová, O. Marsalek, B. Schmidt, and P. Jungwirth, “Peptide salt bridge stability: From gas phase via microhydration to bulk water simulations”, *Journal of Chemical Physics* **2012**, *137*, 185101.
7. O. Marsalek, C. G. Elles, P. A. Pieniazek, E. Pluhařová, J. VandeVondele, S. E. Bradforth, and P. Jungwirth, “Chasing charge localization and chemical reactivity following photoionization in liquid water”, *Journal of Chemical Physics* **2011**, *135*, 224510.
8. C. A. Schroeder, E. Pluhařová, R. Seidel, W. P. Schroeder, B. Winter, M. Faubel, P. Slavíček, P. Jungwirth, and S. E. Bradforth, “Photoelectron spectroscopy of pyrimidine and purine nucleotides and their component parts in buffered aqueous solution”, **2014**, *submitted*.
9. E. Pluhařová, C. A. Schroeder, R. Seidel, S. E. Bradforth, B. Winter, M. Faubel, P. Slavíček, and P. Jungwirth, “Unexpectedly Small Effect of the DNA Environment on Vertical Ionization Energies of Aqueous Nucleobases”, *Journal of Physical Chemistry Letters* **2013**, *4*, 3766—3769.

Attached Publications